

Full length article

Finite element modelling of sheathed cold-formed steel beam–columns

Constantinos Kyprianou^{*}, Pinelopi Kyvelou, Leroy Gardner, David A. Nethercot

Department of Civil and Environmental Engineering, Imperial College London, South Kensington Campus, London SW7 2AZ, UK

ARTICLE INFO

Keywords:

Cold-formed steel
Finite element analysis
Numerical modelling
OSB
Plasterboard
Sheathing

ABSTRACT

The structural behaviour of sheathed cold-formed steel lipped channel section columns (studs) subjected to combined compression and major axis bending is investigated herein by means of numerical modelling. Finite element (FE) models of single studs, set in tracks and connected to oriented strand board (OSB) and gypsum plasterboard sheathing under varying combinations of axial compression and horizontal loading were developed in ABAQUS and validated against experimental results reported in the literature. The developed numerical models incorporated cross-sectional and global geometric imperfections, while geometrical and material nonlinearities for both the steel and the sheathing were considered in the analyses. Particular emphasis was given to replicating the “as-built” boundary conditions at the ends of the columns, controlled by the screws connecting the column to the track and by the column–track contact interaction. The interaction between the sheathing and the column, as well as the behaviour of the fasteners connecting the two components, were also explicitly modelled. Both the shear and pull-through characteristics of the fasteners were considered and simulated based on experimental findings. Following successful validation of the finite element models, parametric studies were conducted. The results showed that substantial structural performance benefits can be achieved by the addition of sheathing to cold-formed steel members and that the spacing of the connectors has a strong influence on the member response. For a typical system, decreasing the connector spacing from 300 mm to 75 mm was found to increase stud capacity and stiffness by up to 12% and 10% respectively when in pure compression and up to 26% and 22% respectively when in pure bending; under combined loading, capacity increases of up to 29% were found.

1. Introduction

Cold-formed steel C-lipped vertical members (studs) set in tracks and sheathed with wood-based boards or gypsum plasterboards are frequently employed in the construction industry, both as non-structural and load-bearing wall systems, offering practicality, economy and versatility. Load-bearing light-steel frames are becoming increasingly popular in buildings exceeding four storeys, with their use being further promoted by the recent emerging practice of lightweight modular construction [1].

It is well understood that column strength can be increased by bracing the member, and since sheathing is present in most load-bearing stud applications, it is logical to utilise its presence structurally [2–15] and potentially eliminate the need for secondary steel bracing members. Therefore, although several studies have been carried out to investigate the structural response of bare cold-formed steel C-lipped members [16–20], others [4–9,11,12] have focused on quantifying the beneficial bracing effect of sheathing on the axial load-bearing capacity of cold-formed steel studs. Nevertheless, research on the possibility

of achieving further performance gains by increasing the number of connectors between the columns and boards has been limited [6–8].

Analytical work [8] on cold-formed steel studs under axial load, sheathed on one or both sides, indicated that no significant benefits can be achieved by decreasing the connector spacing from 600 mm to 300 mm or by using stronger sheathing material, while numerical investigations with plasterboard sheathing on one or both sides of the stud [6,8] indicated further enhancements in capacity could be achieved by decreasing the connector spacing to less than 300 mm. Work on the beneficial influence of sheathing on stud columns under combined compression and major axis bending has been presented in [10], while sheathed specimens under pure bending was the focus in [21].

Finite element models of single sheathed studs or wall systems under compression have been presented in [6,12,13,22] but equivalent models for combined axial and horizontal loading are lacking. Numerical studies to date [6,12,13,22] have adopted a linear elastic material model for the sheathing. In [22], the focus was on the assessment of the shear demand on the screw connectors between the sheathing and the

^{*} Corresponding author.

E-mail addresses: constantinos.kyprianou08@imperial.ac.uk (C. Kyprianou), pinelopi.kyvelou11@imperial.ac.uk (P. Kyvelou), leroy.gardner@imperial.ac.uk (L. Gardner), d.nethercot@imperial.ac.uk (D.A. Nethercot).

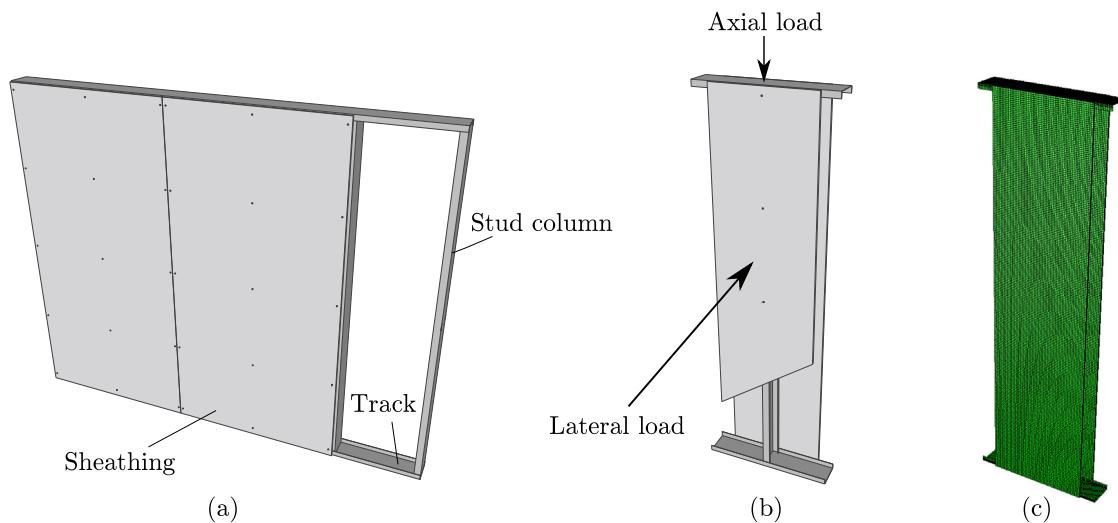


Fig. 1. Illustrations of (a) stud wall with sheathing (b) single sheathed stud column under compression and bending about the major axis (c) finite element model.

steel, while in [12], modelling of user-defined elements to describe the nonlinear response of these screws under monotonic and cyclic loading was presented and evaluated against experimental results.

A sophisticated finite element (FE) model developed for the simulation of stud columns sheathed with OSB and plasterboard is presented in Section 2 of this paper. Models of the screw connection behaviour in pull-through and shear, developed in [23] based on experimental studies [24], are employed herein to capture the connector behaviour observed in the full scale sheathed beam–column tests reported in [25, 26]. After successful validation against experimental data reported in [10,18–20,25–29] (see Section 3), the developed FE model is employed for parametric studies, presented in Section 4, which show that significant performance gains can be achieved by decreasing the spacing of the connectors used to secure various configurations of sheathing to the studs.

2. Finite element modelling

The finite element software ABAQUS [30], which has been extensively used in the past for simulating cold-formed steel members [12, 22,31–34] as well as composite structural systems [35], was employed for the numerical investigation presented herein. The examined structural system, illustrated in Fig. 1, is made up of a single stud column connected to sheathing and tracks, reflecting the boundary and loading conditions experienced by stud columns in sheathed wall systems under compression and bending about the major axis. A single stud column was modelled for computational efficiency since, based on experimental studies, single studs set in tracks and connected to sheathing were shown to accurately reflect the behaviour of stud wall systems consisting of five studs [9]. Note that the conducted finite element simulations were based on the configurations presented in the experimental studies of [10,25], where bending was introduced using a mid-height load and four point loads (simulating uniform distributed loading) respectively. The configurations considered involve OSB or plasterboard fastened to the cold-formed steel columns by means of screws, which are simulated with the use of spring elements. The key features of the developed finite element models as well as the relevant modelling assumptions are presented in the following subsections.

2.1. Element type and meshing scheme

The steel components of the examined system, namely the columns and tracks, were modelled with general purpose quadrilateral four-noded S4R [30] shell elements with reduced integration and hourglass control, while the sheathing boards were modelled using eight-noded

C3D8R [30] solid elements with reduced integration and hourglass control, with an aspect ratio approximately equal to one. The spring elements SPRING1, SPRING2 and SPRINGA [30] were used to model the screwed connectors between steel-to-steel and steel-to-board elements in shear and pull-through, as well as to replicate physical restraints such as contact with the loading surfaces or the presence of the foundation.

Following a sensitivity study to ensure that the arising local and distortional buckling modes could be accurately captured, a refined mesh, aiming at an aspect ratio of 1:1 for the flat regions of the cross-section and never exceeding 4:1 for the corners, was employed for the modelling of the cold-formed steel columns and tracks. Since in practice service openings are often cut in the web of stud members which are deeper than 150 mm, and to allow direct comparisons with experiments on stud columns with service hole openings [25], explicit modelling of these openings was performed — see Fig. 2.

For the board, a mesh size of 10 mm along its width and length was employed to ensure alignment with the nodes of the cold-formed steel columns at every other node. Following a sensitivity study, two layers of elements were employed through the board thickness since no significant improvements in accuracy were achieved by the use of more elements. The employed mesh was able to accurately capture the global bow deformation (i.e. horizontal deflection) of the board during loading, while also being relatively computationally inexpensive. The cross-sectional mesh discretisation of the sheathing and cross-sectional notation for both the stud column and the sheathing are illustrated in Fig. 3, where h is the depth of the stud, b is the flange width, c is the lip length, r is the internal corner radius of the stud, t is the thickness of the stud and t_b is the thickness of the sheathing.

2.2. Material modelling

2.2.1. Cold-formed steel

The material properties assigned to the cold-formed steel components of the systems examined herein and used in the validation of the finite element models were obtained from the respective stress–strain curves reported in [22,25,29,31], which were derived by means of tensile coupon testing. The material properties of the test specimens reported in [25], which also served as the basis for the parametric studies reported in Section 4.2, are summarised in Table 1, where t is the thickness of the steel section; a Poisson's ratio of 0.3 was assumed throughout. To describe the stress–strain behaviour of the stud sections featuring a yield plateau, the material model given by Eq. (1) was

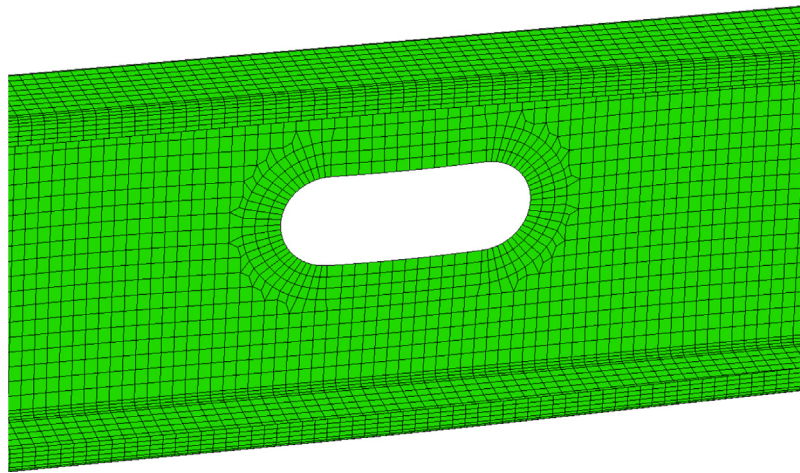


Fig. 2. Adopted finite element mesh for the cold-formed steel columns in the region of a service hole.

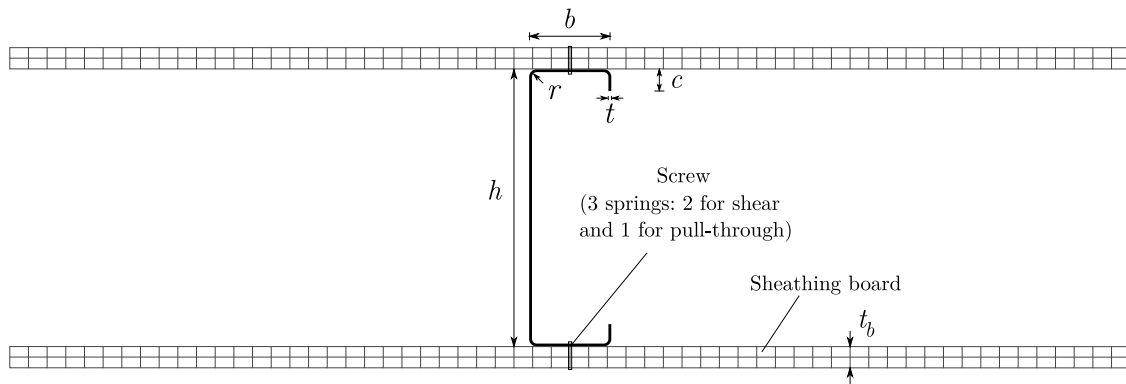


Fig. 3. Cross-sectional notation of stud column and finite element discretisation of sheathing.

Table 1
Average material properties of stud and track reported in [25] and used in the FE model.

Member	<i>t</i> (mm)	<i>E</i> (GPa)	<i>f_y</i> (MPa)	<i>ε_{sh}</i> (%)	<i>f_u</i> (MPa)	<i>ε_u</i> (%)	<i>n</i>
Stud	1.44	204	482	2.38	514	7.90	–
Track	1.18	201	495	1.34	613	13.4	9

employed [36].

$$\sigma = \begin{cases} E\varepsilon & \text{for } \varepsilon \leq \varepsilon_y \\ f_y & \text{for } \varepsilon_y < \varepsilon \leq \varepsilon_{sh} \\ f_y + (f_u - f_y) \left\{ 0.4 \left(\frac{\varepsilon - \varepsilon_{sh}}{\varepsilon_u - \varepsilon_{sh}} \right) + \frac{2 \left(\frac{\varepsilon - \varepsilon_{sh}}{\varepsilon_u - \varepsilon_{sh}} \right)}{\left[1 + 400 \left(\frac{\varepsilon - \varepsilon_{sh}}{\varepsilon_u - \varepsilon_{sh}} \right)^5 \right]^{1/5}} \right\} & \text{for } \varepsilon_{sh} < \varepsilon \leq \varepsilon_u \end{cases} \quad (1)$$

In Eq. (1), σ is the stress, ε is the strain, E is the Young’s modulus, f_y is the yield strength, ε_y is the strain at f_y , ε_{sh} is the strain at the end of the yield plateau, f_u is the ultimate stress and ε_u is the ultimate strain.

Note that for the track sections, which demonstrated a rounded stress–strain profile prior to yield [25], instead of using the linear expression of Eq. (1) up to the yield point, the Ramberg–Osgood model [37,38], given by Eq. (2) was used, where n is an exponent that describes the roundedness of the curve.

$$\varepsilon = \frac{\sigma}{E} + 0.002 \left(\frac{\sigma}{f_y} \right)^n \quad \text{for } \sigma \leq f_y \quad (2)$$

In Fig. 4, typical stress–strain responses of the stud and track sections [25], along with the fitted models (Eqs. (1) and (2)) and their conversion to true stresses σ_{true} and true plastic strains ε_{true}^{pl} using Eqs. (3) and (4) respectively, are presented. Note that no strength enhancements in the corner regions were considered since their influence was deemed to be negligible due to the small thickness t and corner radius r of the modelled cold-formed steel cross-sections.

$$\sigma_{true} = \sigma(1 + \varepsilon) \quad (3)$$

$$\varepsilon_{true}^{pl} = \ln(1 + \varepsilon) - \sigma_{true}/E \quad (4)$$

2.2.2. Plasterboard

Plasterboard displays different stress–strain characteristics in tension and compression, with the ultimate strength in compression f_u being higher by about two to four times compared with that in tension, but with the ultimate strain ε_u at f_u being significantly higher in tension [23]. Plasterboard also displays a degree of anisotropy due to its production process, with the mechanical properties in the longitudinal direction being higher than those in the transverse direction [23,39].

The material models established in [23] were employed herein. The adopted stress–strain behaviour is illustrated in Fig. 5, with the positive

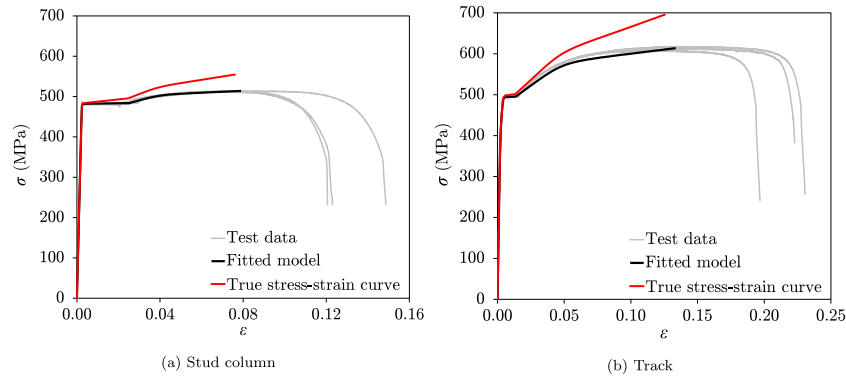


Fig. 4. Stress–strain curves for (a) stud and (b) track.

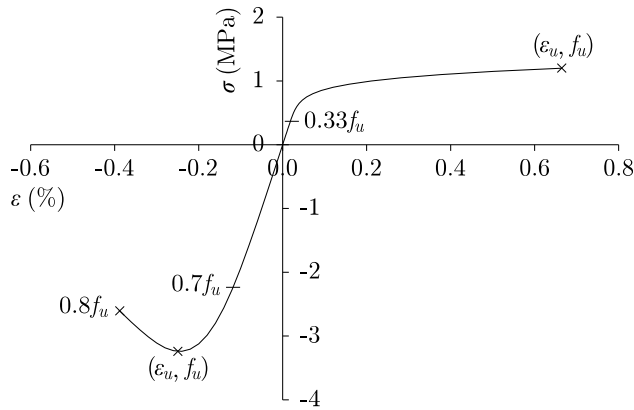


Fig. 5. Uniaxial stress–strain behaviour of plasterboard adopted in finite element models, with positive values signifying tension.

values of stress and strain corresponding to tension and the negative values signifying compression. The nonlinear material behaviour in compression was extended beyond the ultimate capacity f_u , and up to 20% drop after f_u , using the Mander [40] model as demonstrated in [23,39,41]. Note that the material response was assumed to be elastic up to $0.33f_u$ in tension and $0.7f_u$ in compression — see Fig. 5.

The influence of anisotropy in plasterboard material on the overall structural response of the examined systems was investigated by carrying out FE analyses with either the longitudinal or transverse mechanical properties [23,24]. The observed degree of anisotropy reported in [23] for 12.5 mm thick gypsum plasterboard (i.e. 12% difference in elastic modulus and 10% difference in compressive strength) was found to have a negligible impact (less than 2%) on the ultimate compression capacities of the studied systems. The material behaviour was therefore assumed to be isotropic, based on the mean values of the longitudinal and transverse properties reported in [23], which are presented in Table 2.

Table 2
Material properties of plasterboard adopted in FE models.

E (MPa)	ν	Tension			Compression	
		f_u (MPa)	ϵ_u (%)	n	f_u (MPa)	ϵ_u (%)
2010	0.2	1.20	0.665	7.25	3.24	0.245

The evolution of the yield surface, reflecting compressive crushing and tensile cracking of the gypsum, was simulated using the concrete damaged plasticity model in ABAQUS [30], with the model parameters taken as the default ABAQUS [30] values apart from the dilation angle which was taken as $\psi = 11.0$ following sensitivity studies to ensure numerical convergence and good agreement with the experimental

results. In compression, the post-elastic stress–strain behaviour was described using the *CONCRETE COMPRESSION HARDENING [30] function, while in tension the model was adapted to account for the ductile tensile behaviour of the gypsum, by defining the stresses and strains explicitly up to the ultimate tensile strain ϵ_u and stress σ_u using the *CONCRETE TENSION STIFFENING [30] function.

2.2.3. OSB

OSB also displays a degree of anisotropy, but as for the plasterboard, this was found to have a negligible influence on the response of the examined systems, and hence the material properties were taken as the mean values for the longitudinal and transverse directions reported in [23] — see Table 3, while the Ramberg–Osgood formulation provided in [23] was adopted to describe the stress–strain behaviour of the OSB material.

Table 3
OSB material model characteristics.

E (MPa)	ν	Tension	Compression		
		f_u (MPa)	f_u (MPa)	ϵ_u (%)	n
3080	0.2	10.2	12.4	0.56	12

2.3. Modelling of screwed connections

2.3.1. Sheathing-to-steel connection

The self-drilling screws used for the connection between the sheathing boards and the flanges of the steel C-lipped columns were modelled using three 2-noded nonlinear translational springs (SPRING2 [30]) acting in the x , y and z directions, as illustrated in Fig. 6. The spring in the y direction was defined between a node on the steel flange and a node on the outer surface of the sheathing, while the springs in the x and z directions were defined between the respective nodes on the inside surface of the sheathing and the steel flange.

The characteristics of the springs acting along the length and width of the stud-board interface (in z and x direction respectively as per Fig. 6) were defined using the load–slip behaviour of an equivalent screwed connection in shear, while the separation of the two surfaces at the screw (spring) locations (i.e. along y direction) was defined using the pull-through behaviour of an equivalent screwed connection, determined in accordance with the models established in [23]. The derived responses in shear and pull-through are illustrated in Fig. 7 (a) and Fig. 7 (b) respectively, where it can be observed that for the springs describing the shear behaviour of the connection, the same load–slip response was assigned in both directions (to designate the same behaviour in tension and compression), while for the springs describing the pull-through behaviour, load–slip values were defined only in one direction, to activate the springs only when in tension. Note that, due to the nonlinearity of the response assigned to the springs, the stiffness of the connection would be slightly overestimated

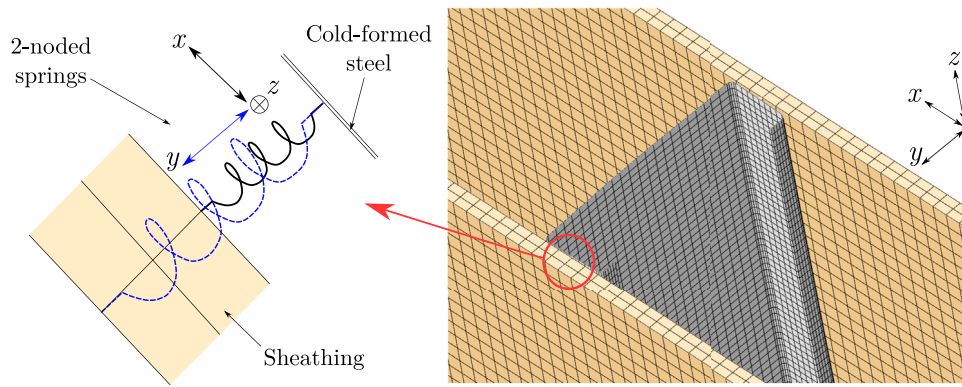


Fig. 6. Simulation of screwed connection between sheathing and cold-formed steel using three 2-noded nonlinear springs.

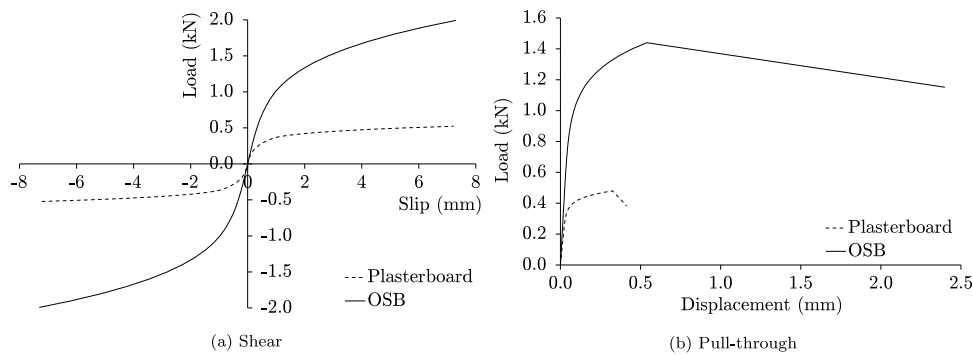


Fig. 7. Adopted load-slip responses for springs in the FE model for simulating sheathing-to-steel (a) shear and (b) pull-through screwed connection behaviour.

for forces acting at an angle to the global axes since more than one spring would be engaged. However, for the systems examined herein, the shear force at the stud-sheathing interface was always found to act along the longitudinal direction (i.e. z axis), thus not affecting the obtained results.

2.3.2. Steel-to-steel connection

The self-driving screws used in practice for the column-to-track connection were modelled using 2-noded nonlinear translational springs (SPRING2) along the longitudinal and transverse column-to-track interfaces. The load-slip response assigned to the springs was derived using a nonlinear bearing deformation curve introduced in [42], and was capped by the shear capacity of the connection $F_{u,v}$, as determined in [24]. The adopted load-slip response of these springs in shear is illustrated in Fig. 8, where positive and negative values designate compression and tension respectively. For the axial behaviour of the screwed connection, a 2-noded linear translational spring, defined along the direction of the length of the screw, was used, with its stiffness set equal to the axial stiffness of the screw EA/L , where A is the cross-sectional area of the screw and L is the sum of the thickness of the stud and track. The ultimate tensile capacity of the screw $F_{u,s}$ was determined in line with the results reported in [24].

2.4. Geometrical imperfections

Cold-formed steel sections are particularly prone to cross-sectional instabilities, such as local and distortional buckling, as well as to global instabilities, such as flexural and flexural-torsional buckling, when unbraced. Initial imperfections that ensure that these modes of buckling are not inhibited were therefore incorporated into the developed FE models. The imperfections were introduced in the form of elastic buckling mode shapes obtained from the finite element strip analysis

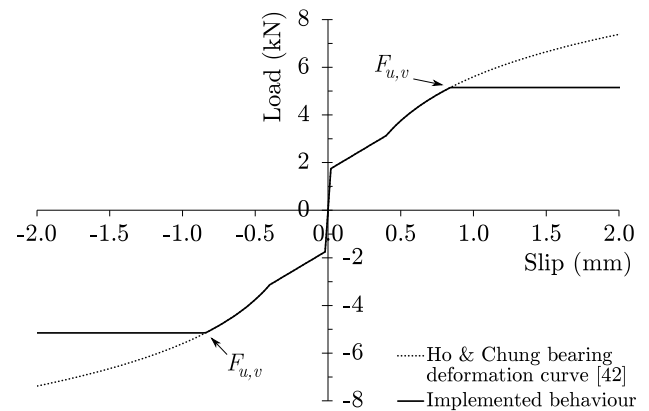


Fig. 8. Adopted load-slip response for springs in the FE model for simulating steel-to-steel screwed connection behaviour in shear.

software CUFISM [43]. Following their determination, the local and distortional modes were longitudinally distributed using sinusoidal functions with periods equal to their corresponding critical wavelengths. Similarly, the global imperfection shapes were introduced using single half-sine and full cosine functions for the flexural and torsional buckling modes, respectively, as recommended in [44] and illustrated in Fig. 9. The distribution of all buckling mode shapes along the length of the steel columns is shown in Fig. 10. All the cross-sectional and global buckling modes were then scaled to a prescribed amplitude and superimposed for implementation in ABAQUS [30]. For the validation studies presented in Section 3, the measured imperfection amplitudes reported in [18,25,27,29] were used in the corresponding models, while for the parametric study presented in Section 4.2, the adopted imperfection amplitudes were based on the values reported in [25].

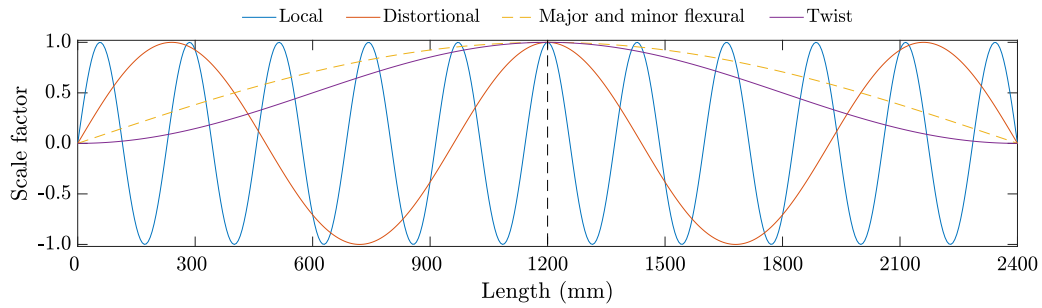


Fig. 9. Shapes of different imperfection modes along member lengths.

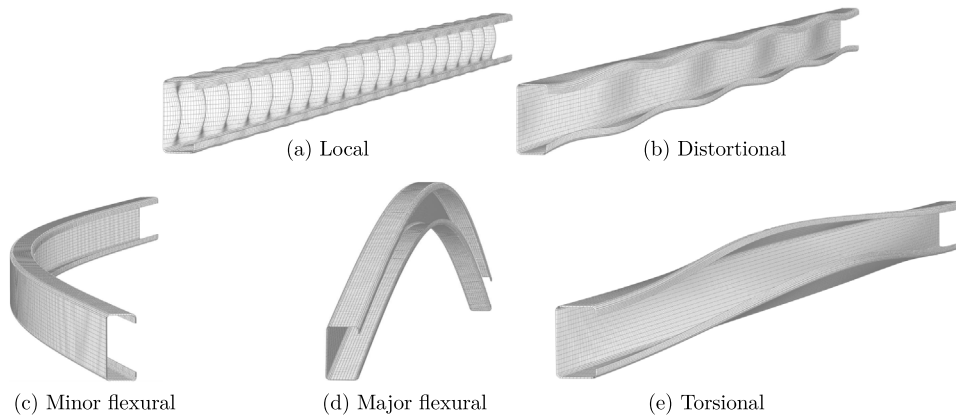


Fig. 10. Illustration of: (a, b) cross-sectional and (c – e) global imperfections.

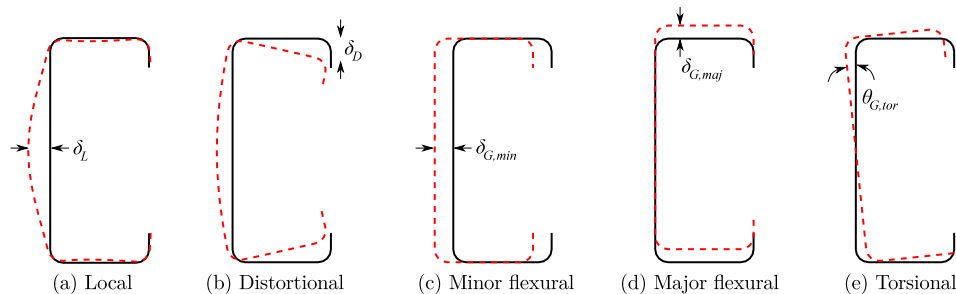


Fig. 11. Mode shape and amplitude notation of: (a, b) cross-sectional and (c – e) global imperfections.

Note that for sheathed specimens, the sheathing boards were also modelled with major and minor flexural imperfections equal to those of the stud in order to ensure that there were no gaps between the stud and the board, as well as alignment of the nodes on the board and steel used for the spring definitions (simulating the screws). The following notation is employed for the imperfection amplitudes: δ_L for local, δ_D for distortional, $\delta_{G,min}$ for minor axis flexural, $\delta_{G,maj}$ for major axis flexural and $\theta_{G,tor}$ for twist; these are illustrated in Fig. 11.

2.5. Boundary and loading conditions

It is common practice for steel columns to be modelled under the assumption of idealised boundaries corresponding to either fully fixed or pinned end conditions. However, since in reality cold-formed steel studs are usually set in tracks, their actual boundary conditions are somewhat different. Both the idealised and realistic end conditions are considered herein.

Idealised boundary conditions were implemented by coupling all the cross-sectional nodes at both column ends to reference nodes located at the respective end centroids, using BEAM Multipoint Constraints (MPCs) [30]. For the simulation of pinned conditions, the rotational degrees of freedom about the major and minor axes were released.

For the finite element models simulating the realistic boundary conditions at the column ends, as tested in [10,25,27], explicit modelling of the tracks, contact with the studs, and the track-to-column connection were all implemented, as shown in Fig. 12. The adopted behaviour of the springs, for the simulation of the screwed connection, was modelled using the description given in Section 2.3.2.

Nonlinear translational springs (SPRING1 type) were positioned under the bottom track, simulating the ground, allowing upward but preventing downward movement. The holding-down anchor bolt shown in Fig. 12 (a), used to secure the track to the ground, was simulated as a pinned constraint (restraining all three translations), as shown in

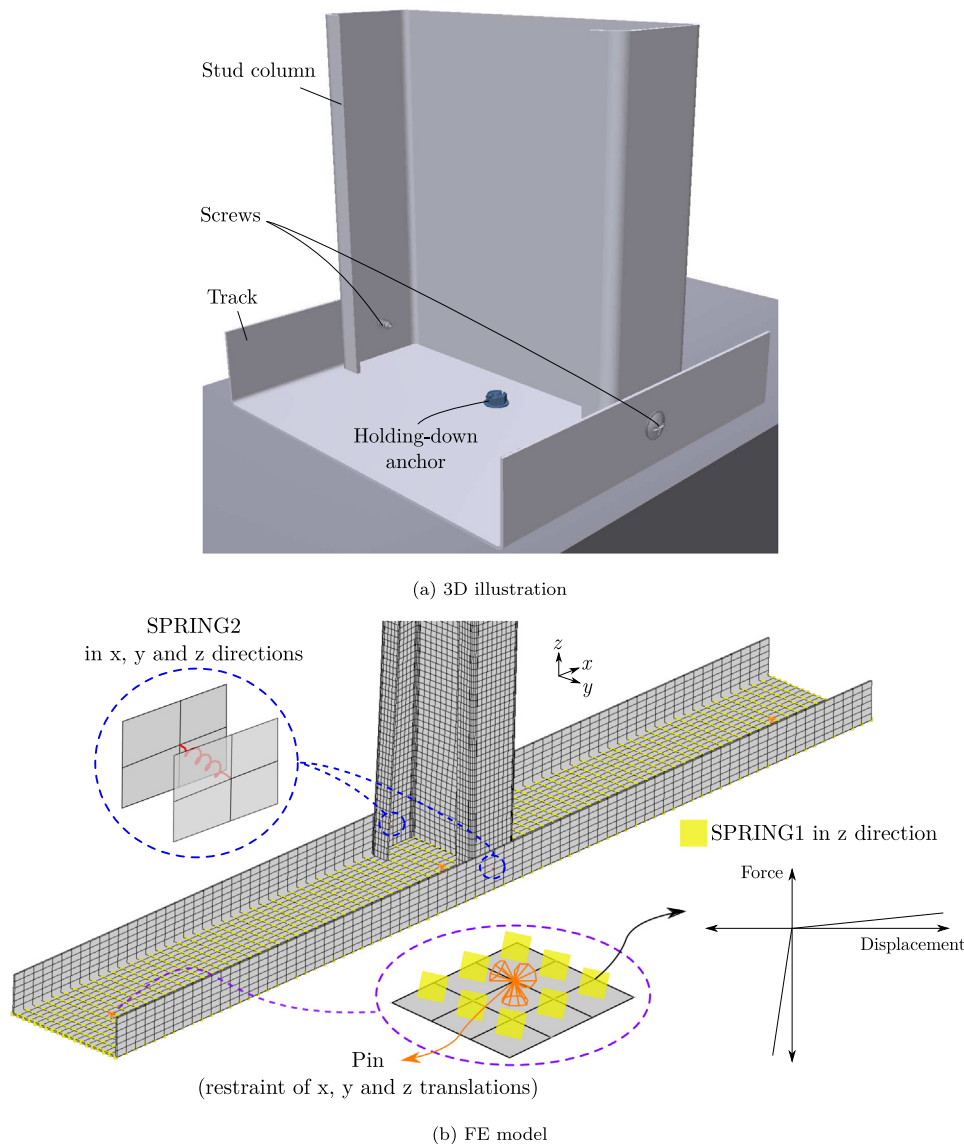


Fig. 12. Column-to-track connection: (a) 3D illustration and (b) FE model.

Fig. 12 (b). Similarly, the use of nonlinear springs at the top track allowed downward movement, by being freely extensible, but prevented upward movement, by being incompressible. Unlike the ground springs which were fixed into position (SPRING1 type), the top springs were 2-noded (SPRING2 type) and connected at their free ends by an MPC to a reference node located at the centre of the track as shown in Fig. 13. For the specimens under pure compression and combined loading, axial loading was introduced through this reference node to the web of the track, only when the nonlinear springs were in compression, simulating the effect of a rigid loading plate at the top of the track. Anchors on the top track used to secure it to the rigid loading plane were simulated with pinned constraints only in the x and y directions, while in the z direction, the *EQUATION command was used to keep the vertical distance between the anchors and the loading point constant.

Similarly, lateral loading was applied to the board surface with the use of nonlinear 2-noded springs (with high stiffness defined when the springs were in compression). As for the springs on the top track, the free ends of the springs were connected with BEAM MPCs to a single reference point, where the load was introduced. To simulate the four-point loading scheme employed in the tests reported in [25],

a whiffle-tree arrangement was modelled using stiff linear 2-noded springs (SPRINGA type) and BEAM MPC elements, connected to a single reference point at mid-height and mid-width of the board, where the lateral load was applied. A schematic illustration of the implementation of the lateral four-point loading scheme is illustrated in Fig. 14.

Note that, since the sheathing boards in the FE model were not directly loaded, their top and bottom ends were free to move, replicating the boundary conditions of the physical tests described in [10,25,27]. In Fig. 15, the end deformations of the modelled column and track at various key stages of the loading are presented, along with the corresponding board deformation. When under pure compression, the incompressible springs transfer the load directly to the web of the track, while, when in bending, the susceptibility of the column-to-track connection to rotation is accounted for by allowing the track to move downwards but preventing it from moving upwards, as such replicating the realistic boundary conditions. The boards, as described in the physical tests reported in [25], were not connected to the tracks but their contact interaction was simulated using springs, which prevented the boards moving towards the tracks but allowed their free movement away from them — see Fig. 15 (c).

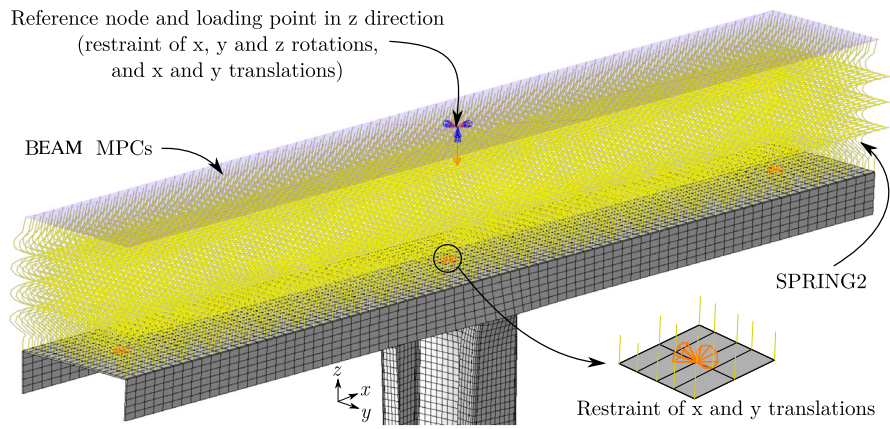


Fig. 13. Column-to-top-track detail and axial loading.

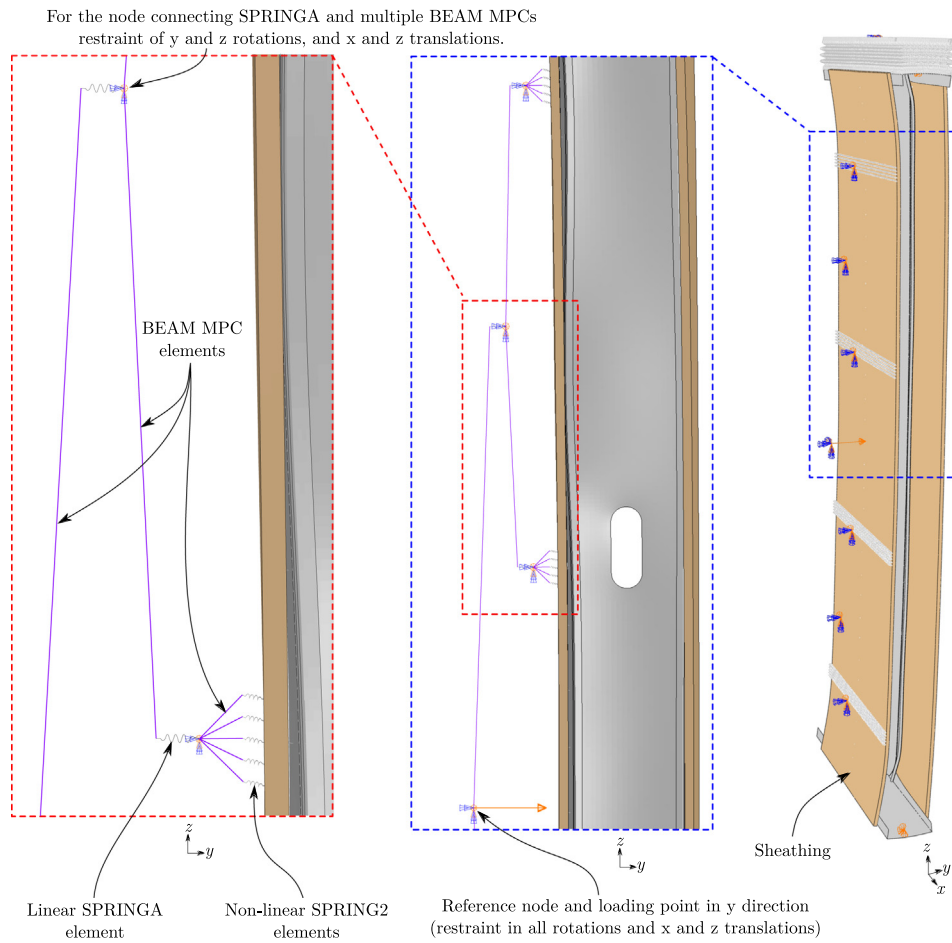


Fig. 14. FE model of four-point loading scheme.

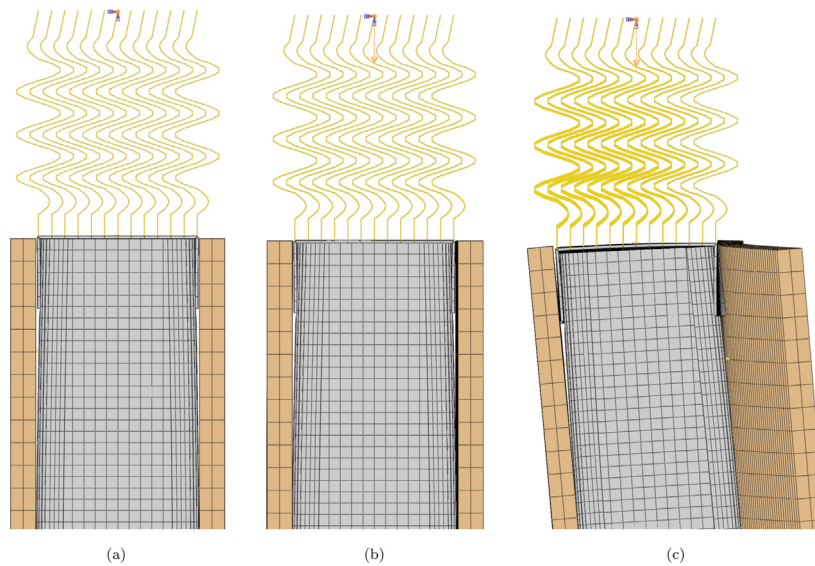


Fig. 15. Stages of typical end deformation from FE model of column and track under combined loading at (a) start of analysis (b) end of compression — Step 1 and (c) end of lateral load (bending) – Step 2.

2.6. Contact interaction and solution scheme

The contact interaction between the column and the tracks was implemented using the generalised contact algorithm in ABAQUS (*CONTACT INCLUSIONS) [30], while the interaction between the column and the boards was defined using the contact pair algorithm (*CONTACT PAIR) [30]. “Hard contact” was defined in the normal direction ensuring no surface overlapping, and a friction coefficient of 0.2 [45] was employed in the tangential direction. Both geometric and material nonlinearities were accounted for in the analyses performed. For the finite element analyses where idealised fully fixed and pinned bare steel columns were modelled, the modified static Riks [30] solver was employed. However, for the simulation of the more complicated systems (i.e. specimens in tracks with single or double sheathing), the use of the general static solver with artificial stabilisation was necessary to achieve convergence.

For the combined load cases, compression was initially introduced using a geometrically nonlinear static analysis in load control, followed by a second load step where horizontal loading was introduced using displacement control in conjunction with the general static solver and artificial stabilisation, with a set limit of stabilisation to strain energy equal to 0.01. For the combined loading scenarios, the *MODEL CHANGE ADD and *MODEL CHANGE REMOVE commands [30] were used between the two load steps (with the first load step corresponding to the axial loading of the column and the second to the lateral loading), to add the lateral springs associated with the whiffle-tree and to replace the top track springs with undeformed ones. The position of the top axial reference node and the compression load remained constant during the second load step. Replacement of the top track springs was performed so that, with the onset of bending (i.e. load step 2), the top springs would not be in an already compressed phase (achieved during step 1) but in their neutral state.

3. FE model validation

Validation of the developed FE models against test results from four different studies, is presented herein. A summary of the configurations and loading conditions of the modelled specimens is presented in Table 4. In total, 56 physical tests were employed for the validation process, of which 42 were loaded in pure compression [18,25,28], 11 under combined loading [25,29] and 3 in pure bending [25]. The selected pool of tests varied in section size, length, sheathing

configuration, boundary conditions and loading conditions. Detailed comparisons between the test and FE results are reported in [26], while a summary is provided herein.

3.1. Studs under compression

A summary of the 42 pure compression studies considered and comparisons between the ultimate compression capacities attained by the test specimens $P_{u,exp}$ and those predicted by the finite elements models $P_{u,FE}$ are presented in Table 5.

3.1.1. Bare studs with either fully fixed or pinned boundary conditions

For the first set of validation models, a series of tests [18] on bare cold-formed steel C-lipped shaped columns of different lengths and cross-section sizes was simulated, with the end boundaries either fully fixed or pinned. Measured material stress–strain curves, specimen dimensions and geometric imperfections, as reported in [18–20,31], were employed in the conducted finite element simulations. Comparisons between the ultimate compression capacities attained by the test specimens $P_{u,exp}$ [18] and those predicted by the finite elements models $P_{u,FE}$ are presented in Table 5, with a mean $P_{u,exp}/P_{u,FE}$ ratio of 1.03 and a coefficient of variation (COV) of 0.04. The finite element models were also found capable of accurately capturing the exhibited failure modes as well as the recorded load–axial shortening curves, as shown in Fig. 16.

3.1.2. Studs with various sheathing configurations set in tracks

The second considered set of tests [28] allowed validation of the model in which the end tracks were explicitly simulated, as described in Section 2.5. Twenty physical tests on studs set in tracks of various lengths and sheathing configurations, as reported in [27,28], were utilised. Measured cross-sectional dimensions [27], material properties [22] and initial imperfections [27] were incorporated into the numerical simulations, while for all sheathed specimens a connector spacing of 300 mm was employed. The observed failure modes were captured (including local, distortional, flexural and flexural–torsional buckling, as reported in [27]) by the finite element models. Comparisons between the FE and test results are presented in Table 5, where a mean $P_{u,exp}/P_{u,FE}$ ratio of 0.96 was obtained for all the examined systems. In order to examine the influence of the adopted boundary conditions (i.e. explicit modelling of the end tracks) on the load-carrying capacity of the studs, finite element analyses of the same

Table 4
Summary of studies and types of specimen used for the FE model validation.

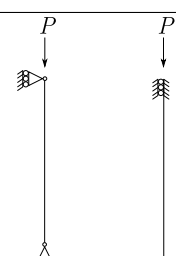
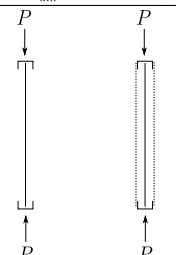
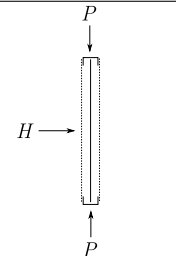
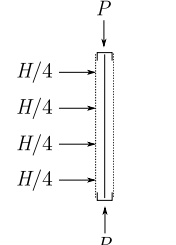
Study	Loading	No. of tests	Configuration	
[18]	Compression	14	Bare studs with ideal boundaries (pinned and fixed)	
[28]	Compression	4 16	Bare studs set in tracks Sheathed studs set in tracks	
[29]	Combined loading	5	Sheathed studs set in tracks	
[25]	Compression Combined loading Bending	8 6 3	Sheathed studs set in tracks	

Table 5
Comparison between FE and test results for specimens loaded in compression reported in [18,25,28].

Study	No. of tests	Sheathing	Screw spacing (mm)	Boundaries	$P_{u,exp}/P_{u,FE}$	
					Mean	COV
[18]	10	No sheathing	N/A	Fixed-Fixed	1.03	0.05
	4	No sheathing	N/A	Pinned-Pinned	1.02	0.03
[28]	4	No sheathing	N/A	Tracks	0.93	0.07
	4	OSB-Bare	300	Tracks	0.99	0.03
	4	Plasterboard-Plasterboard	300	Tracks	0.95	0.07
	4	OSB-Plasterboard	300	Tracks	0.95	0.04
[25]	4	OSB-OSB	300	Tracks	1.00	0.01
	2	Plasterboard-Plasterboard	600	Tracks	0.96	0.08
	2	Plasterboard-Plasterboard	300	Tracks	1.01	0.05
	1	Plasterboard-Plasterboard	150	Tracks	0.95	-
	1	Plasterboard-Plasterboard	75	Tracks	1.00	-
	1	OSB-OSB	600	Tracks	0.96	-
	1	OSB-OSB	75	Tracks	0.97	-
Weighted average					0.99	0.05

specimens but with idealised fixed boundaries were also carried out, where a mean $P_{u,exp}/P_{u,FE}$ ratio of 0.95 was obtained. The minor discrepancy of 1% in the mean values of ultimate capacities obtained for the two alternative boundary conditions indicates that, when under pure compression, the assumption of idealised fully fixed boundary conditions for a cold-formed steel stud in tracks is realistic.

The third set of validation models were based on the eight tests of studs under pure compression reported in [25]. A summary of the details of boundary conditions, sheathing and screw spacing configuration is provided in Table 5 along with a comparison of the test and FE results, where a mean $P_{u,exp}/P_{u,FE}$ ratio of 0.98 and a COV of 0.04 was obtained. The specimens were 2.4 m long, while the

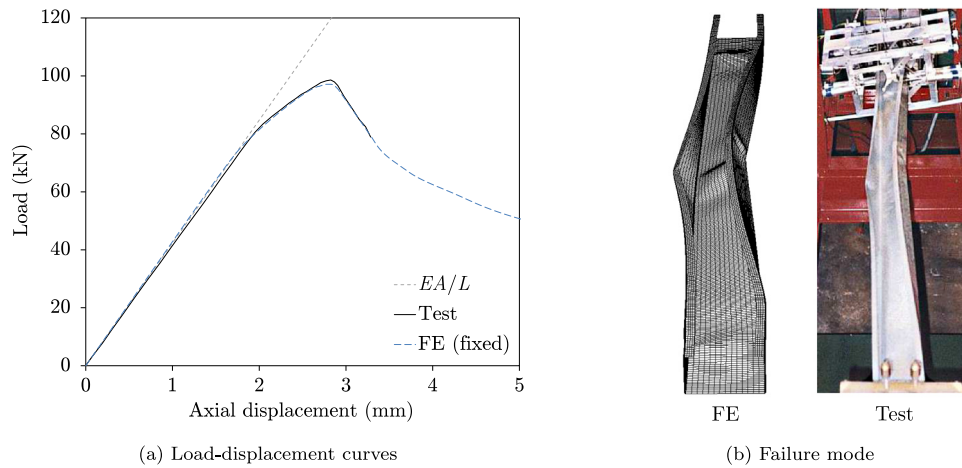


Fig. 16. Typical comparison between the results from the developed FE model and the tests from [18]; example shown is L48F1500 (a lipped channel with flange width 48 mm, 1.5 m long and fully fixed ends).

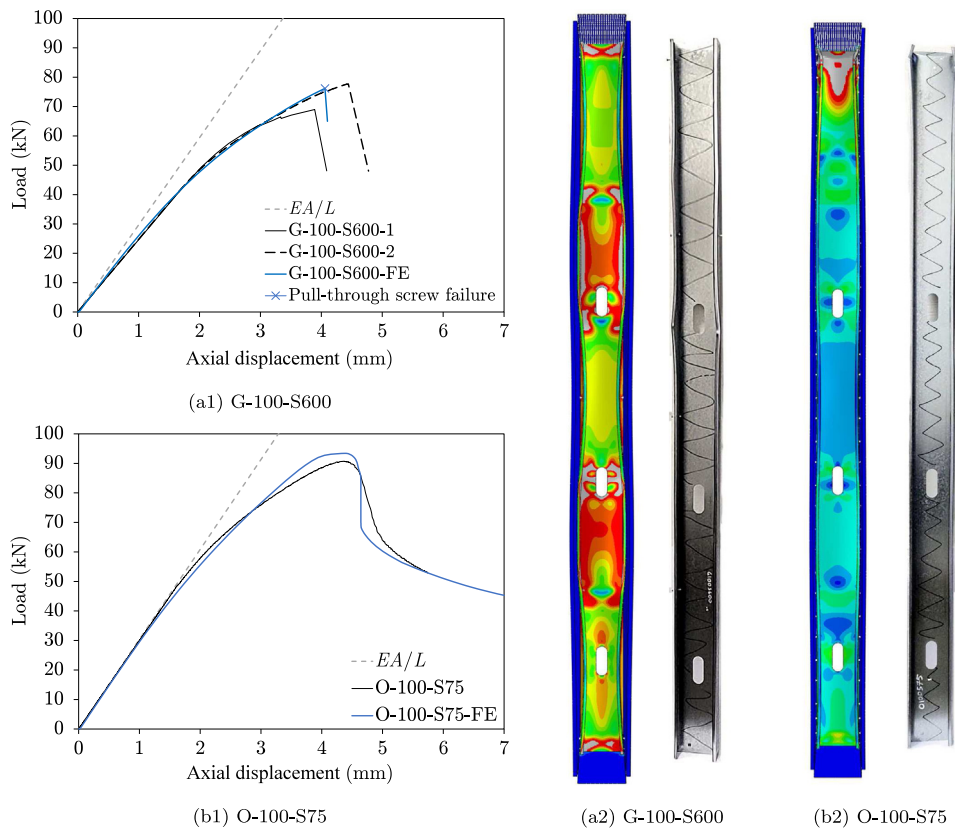


Fig. 17. Comparisons between FE and test results from [25], with subfigures (a1, b1) providing axial load–displacement curves, and (a2, b2) failure modes for plasterboard-sheathed members with screws at 600 mm spacings [G-100-S600] and OSB-sheathed members with screws at 75 mm spacings [O-100-S75] respectively.

dimensions of their C-lipped shaped cross-section were based on the mean measurements reported in [25]. Material nonlinearity for the steel and sheathing was implemented as described in Section 2.2 and initial geometric imperfections as described in Section 2.4 with the adopted imperfection amplitudes based on the measurements reported in [25] and the sensitivity studies described in [26].

Typical comparisons between the FE and test axial load–displacement curves for the specimens under pure compression reported in [25] are presented in Figs. 17 (a1) and (b1) for the plasterboard-sheathed members with screws at 600 mm spacings (G-100-S600) and the OSB-sheathed members with screws at 75 mm spacings (O-100-S75) respectively, where it is demonstrated that the

initial axial stiffness (EA/L) and the overall curve profile are accurately captured. As indicated by the accompanying Figs. 17 (a2) and (b2), the FE models were also found to be capable of capturing the exhibited failure modes accurately. In order to capture pull-through failure in the numerical simulations of the specimens with screw spacings of 600 mm and 300 mm, the pull-through load capacity of the screws in plasterboard, was halved to reflect the fact that, during axial loading of the column, initiation of global buckling about the minor axis results in shear slipping of the screws, causing loss of contact between one side of the screw shank and the inner core of the board. This effect gets magnified with decreasing numbers of screws and at the mid-height of the column where the resulting bow is at its maximum.

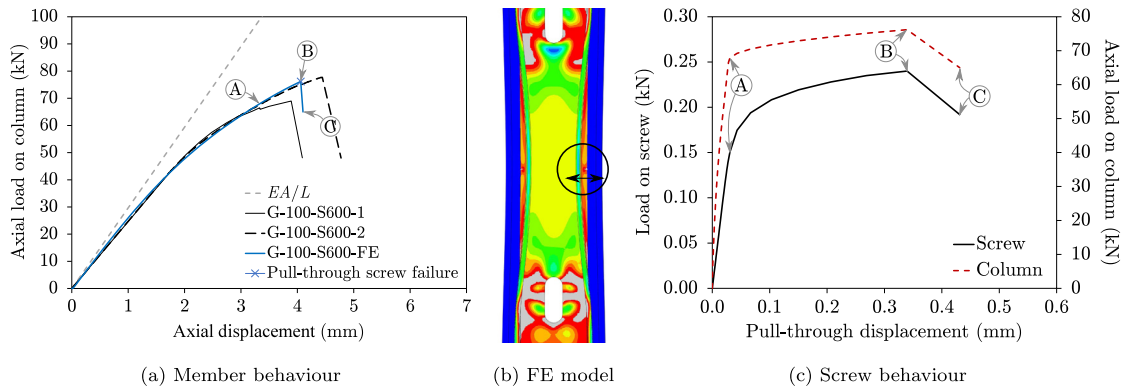


Fig. 18. Illustration of pull-through connector failure, where points A to C are indicated on (a) an axial load–displacement FE curve of the column, (b) FE model detail and (c) a combined graph of two curves consisting of the pull-through screw load and the axial load of the column, both plotted against the pull-through displacement of the screw.

Table 6
Comparison between FE and test results for specimens under combined compression and bending reported in [10,25].

Study	No. of tests	Axial loading level (%) ^a	Sheathing	Connector spacing (mm)	$H_{u,exp}/H_{u,FE}$		R_{exp}/R_{FE}	
					Mean	COV	Mean	COV
[29]	5	80, 60, 50, 30, 10	OSB–OSB	300	0.99	0.06	1.00	0.01
[25]	3	75, 50, 25	OSB–OSB	600	1.06	0.01	1.01	0.01
	3	75, 50, 25	OSB–OSB	75	1.05	0.02	1.01	0.01

^aExpressed as a percentage of the predetermined experimental axial capacity P_u of the specimen.

The pull-through load–displacement behaviour of the critical screw at the mid-height of specimen G-100-S600 is illustrated in Fig. 18, where the key stages are also highlighted with regards to the overall axial load–displacement behaviour of the column.

3.2. Sheathed studs under combined loading

To account for the combined effect of compression P_u and horizontal actions H_u , a resultant force R was calculated using Eq. (5) to facilitate comparisons between the test and FE results. A summary of the combined load test and FE results is presented in Table 6.

$$R = \sqrt{P_u^2 + H_u^2} \tag{5}$$

3.2.1. Sheathed studs under combined compression and mid-height loading

For sheathed stud wall specimens loaded both axially and horizontally, five tests from the study in [10,29] were utilised for the FE model validation; the specimens were sheathed on both sides with OSB, connected using screws of 4.8 mm diameter at a spacing of 300 mm. The specimens tested were first axially loaded to a predetermined load level (see Table 6), calculated based on the results obtained in [27], and then laterally loaded at mid-height until failure, using a line load across the board.

The horizontal line load at mid-height was simulated by a series of springs and a single BEAM MPC element, which is a simplified version of the 4-point loading scheme explained in Section 2.5. The measured cross-sectional dimensions, initial imperfections and material stress–strain curves reported in [29] were incorporated into the FE model. Following the test procedure, the FE models were first loaded to the prescribed axial load level and then loaded horizontally until failure. A comparison between the compressive P_u and horizontal H_u forces attained by the test specimens and predicted by the FE models is illustrated in Fig. 19. As shown in Fig. 19 and reflected by the mean $H_{u,exp}/H_{u,FE}$ and R_{exp}/R_{FE} ratios of 0.99 and 1.00 (see Table 6), there is excellent agreement between the test and FE results.

Accurate replication of the observed failure modes for all specimens under combined loading [10] was achieved by the FE models — see Fig. 20 (b). A typical comparison between the horizontal load–displacement curves from the tests and FE models is presented in

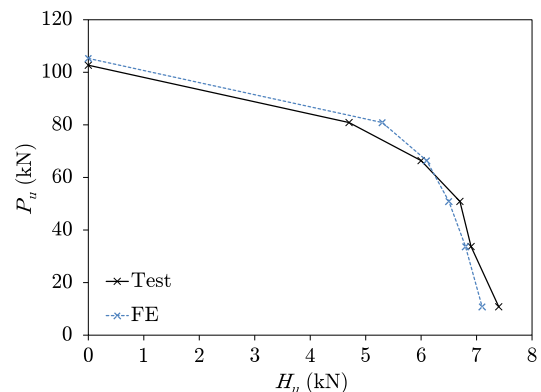


Fig. 19. Comparison between ultimate compression P_u and horizontal H_u loads from the developed FE model and the tests from [10,29] for beam–columns sheathed with OSB and connected at 300 mm intervals.

Fig. 20 (a), where the initial stiffnesses of the curves match that of the theoretical response of the member with pinned boundaries. Note that the screw connector between the loaded side of the sheathing and the steel column at mid-height, where local buckling occurred, suffered pull-through beyond the peak load level, as reported in [10] and illustrated in Fig. 20 (b).

3.2.2. Sheathed studs under combined compression and four-point horizontal loading

The tests under combined axial compression and four-point horizontal loading reported in [25] and summarised in Table 6 are utilised for the further validation of the FE models. Material nonlinearity was implemented as described in Section 2.2 and initial geometric imperfections as described in Section 2.4 with the adopted imperfection amplitudes based on the measurements reported in [25]. These specimens were OSB sheathed and had two different screw connector spacings — at 600 mm and 75 mm. Load application in the FE model followed that of the tests, where specimens were initially compressed at 75%, 50% and 25% of their compressive capacity and then horizontally

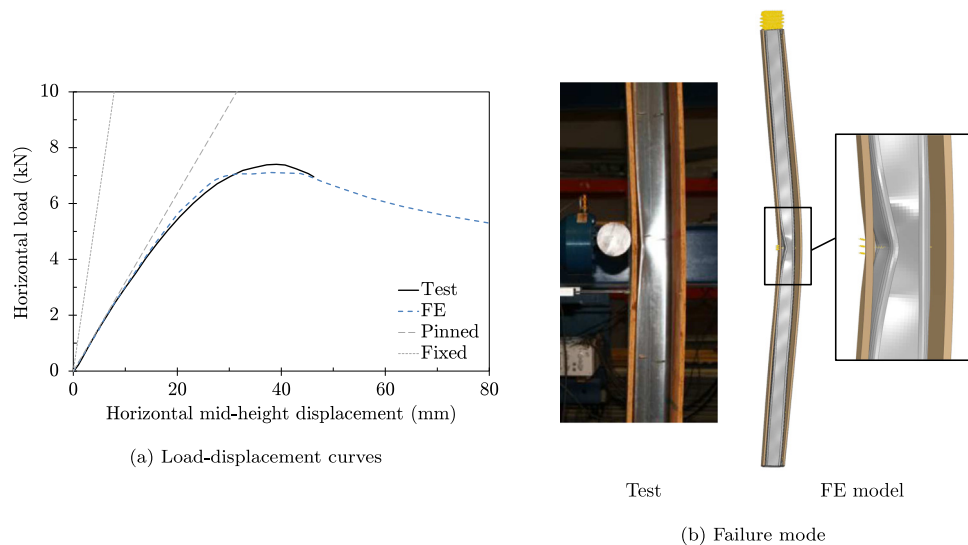


Fig. 20. Typical comparison between the results from the developed FE model and the tests from [29]; the example shown is sheathed with OSB and loaded axially at 10% of $P_{u,exp}$ prior to horizontal loading.

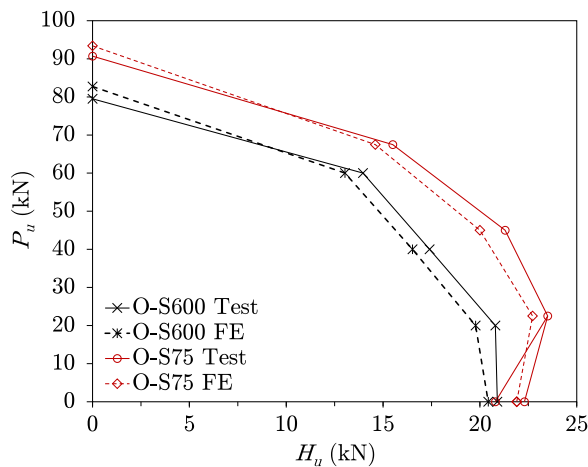


Fig. 21. Comparison between the ultimate compressive P_u and horizontal H_u loads determined from the developed FE models and the tests reported in [25].

loaded until failure. A comparison between the FE and test compression P_u and horizontal H_u ultimate values is presented in Fig. 21, illustrating excellent agreement, with a mean R_{exp}/R_{FE} ratio of 1.01 and a COV of 0.01 — see Table 6. Note that Fig. 21 includes the pure compression and pure bending values for completeness.

The test and FE horizontal load–deflection curves compare well in terms of initial stiffnesses and peak capacities. It should be noted that the initial stiffness of the load–deflection curves is close to the theoretical pinned limits, while a slight increase in fixity is demonstrated with decreasing screw spacing (from 600 mm to 75 mm) and with increasing pre-compression. The FE models were also capable of capturing accurately the observed test failure modes. Typical examples of horizontal load–deflection curves and failure modes are illustrated in Fig. 22 for the specimens compressed at 75% of the compression load with screw spacings of 600 mm (O-75-S600) and 75 mm (O-75-S675). Note that Fig. 22 displays only the bending part of the response of the highly pre-compressed members (at 75% of P_u) and, thus the deviations between the FE and test results close to H_u are not as significant for the overall combined effect measured with the resultant force R .

3.3. Sheathed studs under bending

For specimens under pure bending, the same FE model as in Section 3.2.2 was used. The three tests reported in [25] and summarised in Table 7 are utilised to validate the model, where a mean $H_{exp}/H_{u,FE}$ ratio of 1.00 and a COV of 0.04 was obtained. The ultimate resistance from the FE model was limited by the shear capacity of the column-to-track screw, in agreement with the physical tests. The shear load–slip behaviour of the critical column-to-track screw is illustrated in Fig. 23, where the key points are highlighted with reference to the overall horizontal load–deflection behaviour of the column.

Table 7

Comparison between FE and test results for specimens under pure bending reported in [25].

Study	No. of tests	Sheathing	Connector spacing	$H_{u,exp}/H_{u,FE}$	
				Mean	COV
[25]	1	OSB–OSB	600 mm	1.02	–
	2	OSB–OSB	75 mm	0.98	0.05

4. Parametric studies

Following validation of the developed FE models, parametric studies were undertaken to investigate the influence of the sheathing, spacing of sheathing-to-stud fasteners and section depth on the load-bearing capacity of the examined specimens under various loading scenarios.

4.1. Effect of sheathing

The effect of sheathing type and fastener spacing on the compression capacity of sheathed stud members is investigated in this sub-section. As shown in Table 8, three different sheathing configurations have been assessed, all benchmarked against their equivalent unsheathed response. All specimens were 2.7 m long, while their cross-sectional dimensions were set to: $h = 100$ mm, $b = 44$ mm, $c = 12$ mm, $r = 2.5$ mm and $t = 1.46$ mm — see Fig. 3 for the adopted notation. The material properties of the cold-formed steel studs were taken from [22], while the employed imperfection amplitudes, as shown in Fig. 11, were taken as the recommended 50%ile values from [46]. Therefore, with reference to Fig. 11, $\delta_L = 0.31t$, $\delta_D = 0.75t$, $\delta_{G,min} = L/2910$, $\delta_{G,maj} = L/4010$ and $\theta_{G,tor} = 0.3$ deg/m, where t is the nominal thickness and L is 2.7 m. The material behaviour of the plasterboard and OSB was

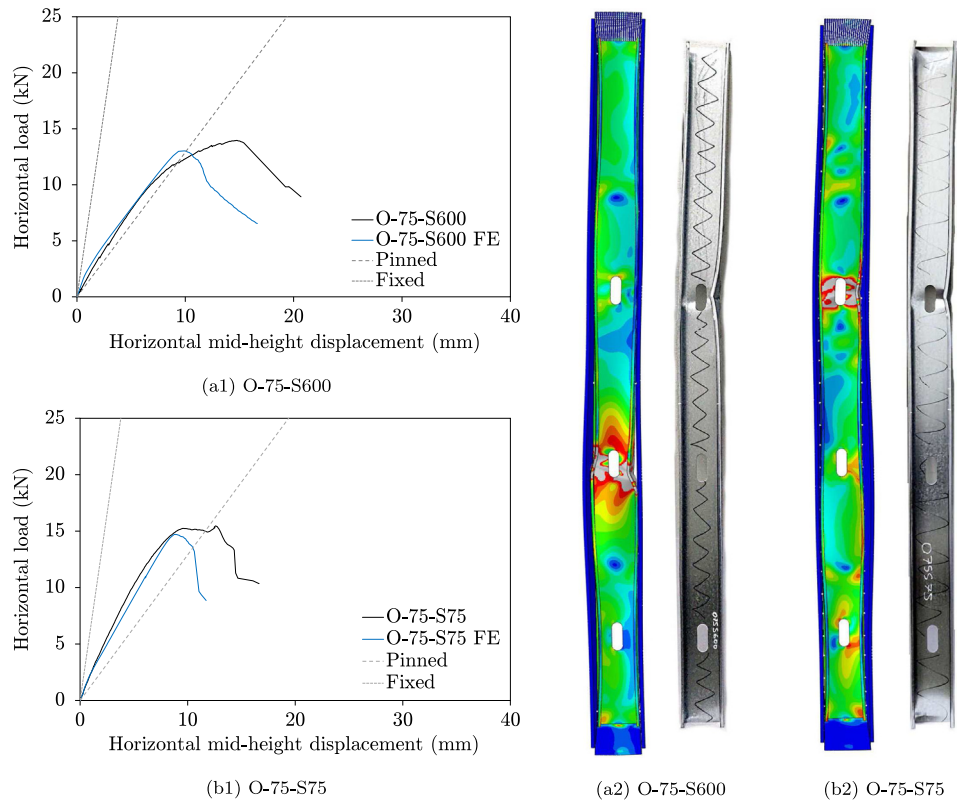


Fig. 22. Comparison between the FE and test horizontal load–displacement curves for OSB sheathed specimens, connected with screws at a spacing of (a1) 600 mm and (b1) 75 mm after being axially loaded to 75% of their compressive capacity; subfigures (a2) and (b2) illustrate the respective failure modes.

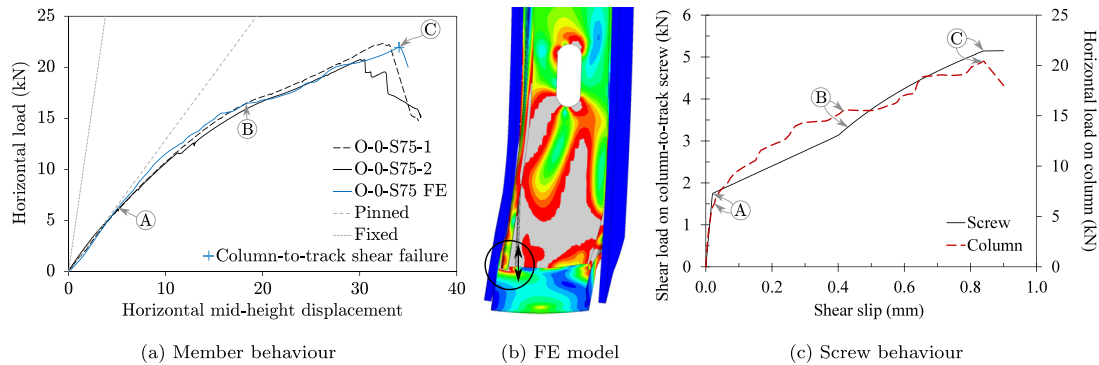


Fig. 23. Illustration of column-to-track shear connector failure for a member in pure bending, where points A to C are indicated on (a) a mid-height horizontal load–displacement FE curve of the column, (b) FE model detail and (c) a combined graph of two curves consisting of the shear load on the screw and the horizontal load of the column, both plotted against the shear slip of the screw.

modelled as reported in Sections 2.2.2 and 2.2.3 respectively, while the modelling of the screw fasteners is described in Section 2.3.1. A comparison of the load–axial shortening curves of the studied systems is shown in Fig. 24. The identification system of the specimens begins with two letters corresponding to the type of sheathing board on each side of the stud (with B = bare, G = plasterboard (gypsum) and O = OSB), followed by the employed fastener spacing in mm.

The FE results showed that adding sheathing to one side of the stud columns led to an increase in capacity of about 30% over the capacity of the bare steel column $P_{FE, BB}$, while for sheathing on both sides, the capacity rose by about 80%–100%. The more robust OSB material yielded greater gains than the plasterboard. The primary reason for the increase in capacity was the restraint against minor axis flexural and flexural–torsional buckling afforded to the columns through the sheathing and fasteners. Greater gains were achieved however for the closer connector spacing (i.e. moving from 300 mm to 100 mm); this is

attributed to the mobilisation of composite action between the boards and the column as well as to a reduction in the wavelength of the distortional buckles.

Table 8
Description and key results of examined systems in FE parametric study.

Specimen	Sheathing	Spacing of fasteners (mm)	P_{FE} (kN)	$P_{FE}/P_{FE, BB}$
BB	Bare–Bare	–	43.2	1.00
GB-S300	Gypsum–Bare	300	53.0	1.23
GB-S100	Gypsum–Bare	100	58.0	1.34
OB-S300	OSB–Bare	300	58.2	1.35
OB-S100	OSB–Bare	100	64.3	1.49
GG-S300	Gypsum–Gypsum	300	76.7	1.78
GG-S100	Gypsum–Gypsum	100	82.0	1.90
OO-S300	OSB–OSB	300	82.0	1.90
OO-S100	OSB–OSB	100	88.1	2.04

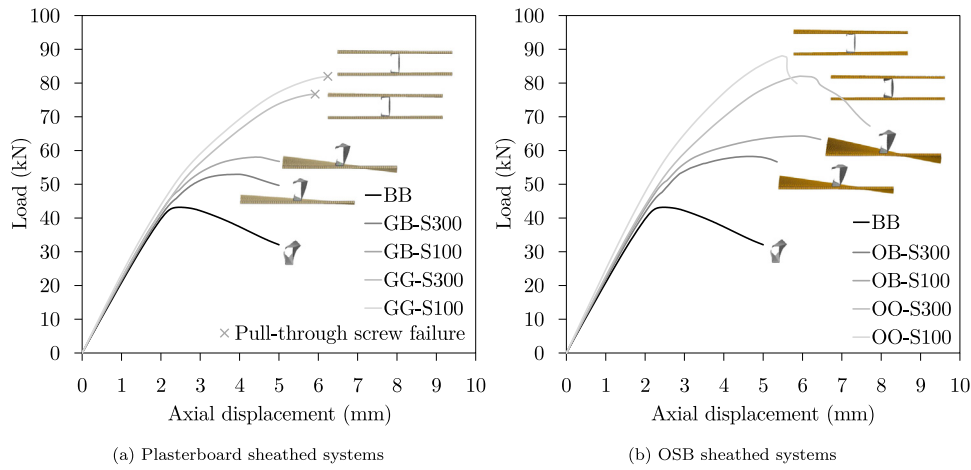


Fig. 24. Comparison of FE load-axial shortening curves for bare steel stud and (a) plasterboard or (b) OSB sheathed systems.

4.2. Effect of connector spacing and section depth

The influence of fastener spacing and section depth on the response of specimens set in tracks and sheathed on both sides with OSB boards is reported in this subsection. The modelled members were studied in pure compression, pure bending and under various combinations of axial and horizontal loading. All specimens were 2.4 m long, while their cross-sectional dimensions were set to $b = 44$ mm, $c = 12$ mm, $r = 2.5$ mm and $t = 1.46$ mm, with a varying section depth $h = 68, 100, 150, 201$ and 252 mm – see Fig. 3 for the adopted notation. Note that for the members with the deeper sections (i.e. $h = 150, 201$ and 252 mm), three service holes were modelled along the stud length. The employed connectors were screws of 4.8 mm in diameter, while the three different connector spacings that were examined were 300 mm, 150 mm and 75 mm, connecting an OSB board of 11 mm thickness to the steel stud. The material properties assigned to the cold-formed steel members and OSB boards were as described in Section 2.2. The modelled tracks were 800 mm long and the boards were 600 mm wide, while the lateral load was introduced using the 4-point loading scheme described in Section 2.5. Modelling of the imperfections was

implemented as described in Section 2.4 using the magnitudes reported in [25], while the screw fasteners were modelled as described in Section 2.3.

A summary of the obtained results is provided in Table 9. The adopted specimen notation starts with the section depth in mm, followed by the nominal thickness of the cold-formed steel member in mm multiplied by 10, then by a hyphen (-) and the letter S and, finally, by the connector spacing in mm. Note that, in the notation of the specimens with depths of 68 mm, 201 mm and 252 mm, these were rounded to 70, 200 and 250 respectively.

4.2.1. Pure compression results

The axial load-displacement curves of all specimens under pure compression are presented in Fig. 25. It can be observed that the initial axial stiffness (EA/L) increases with increasing section depth and decreasing connector spacing, but the stiffness reduces at relatively low load levels for the deeper sections due to the earlier onset of elastic local buckling. The influence of the connector spacing on the ultimate axial capacity P_u and measured initial axial stiffness K_p of the examined systems is schematically illustrated in Figs. 26 and 27 respectively,

Table 9

Key results of the examined systems in the FE parametric studies with varying section depth from 70 mm to 250 mm and fastener spacing from 300 mm to 75 mm under pure compression, pure bending and under various combinations of axial and horizontal loading.

Specimen	Pure compression	0.75 P_u followed by bending		0.5 P_u followed by bending		0.25 P_u followed by bending		Pure bending
	P_u (kN)	0.75 P_u (kN)	H_u (kN)	0.5 P_u (kN)	H_u (kN)	0.25 P_u (kN)	H_u (kN)	H_u (kN)
7015-S300	92.5	69.4	3.2	46.2	5.8	23.1	7.2	8.3
7015-S150	96.2	72.2	3.8	48.1	6.3	24.1	8.0	9.3
7015-S75	99.7	74.8	4.1	49.8	6.8	24.9	8.9	10.5
10015-S300	99.5	74.6	6.1	49.7	10.1	24.9	13.2	15.3
10015-S150	102.8	77.1	6.6	51.4	11.0	25.7	14.3	16.5
10015-S75	103.7	77.8	7.8	51.9	13.1	25.9	16.6	18.8
15015-S300	92.0	69.0	9.5	46.0	15.8	23.0	20.2	23.1
15015-S150	94.3	70.7	10.4	47.1	17.4	23.6	22.1	25.1
15015-S75	95.8	71.9	11.8	47.9	19.6	24.0	24.5	27.9
20015-S300	96.6	72.5	12.6	48.3	21.0	24.2	26.2	29.4
20015-S150	100.3	75.2	13.6	50.2	22.6	25.1	28.8	32.8
20015-S75	103.2	77.4	14.9	51.6	24.9	25.8	31.7	36.1
25015-S300	99.2	74.4	15.1	49.6	25.1	24.8	31.7	35.9
25015-S150	108.3	81.2	16.4	54.2	27.3	27.1	34.5	39.0
25015-S75	110.9	83.2	17.7	55.4	29.6	27.7	37.5	42.5

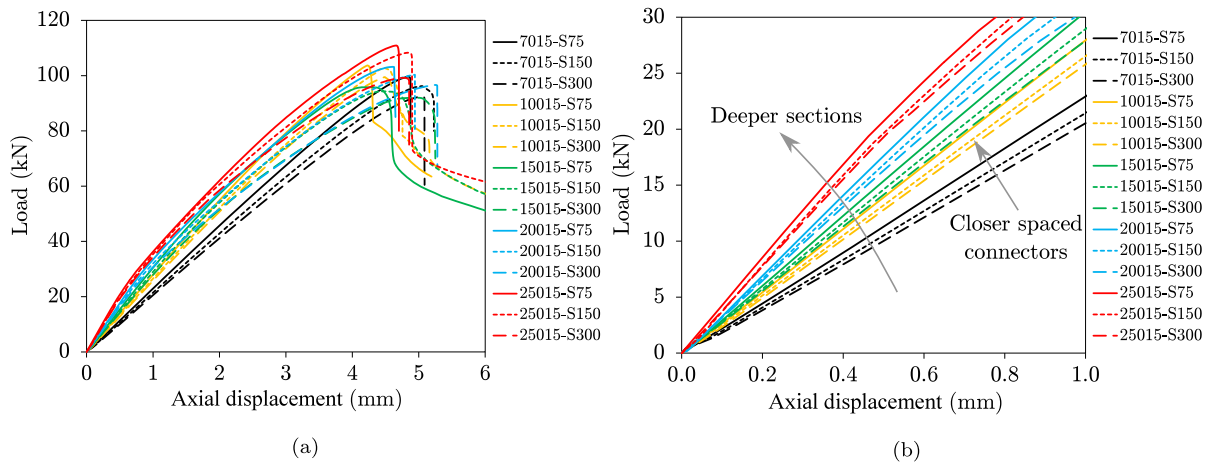


Fig. 25. FE parametric axial load–displacements curves for sheathed members in compression: (a) full spectrum and (b) initial detail.

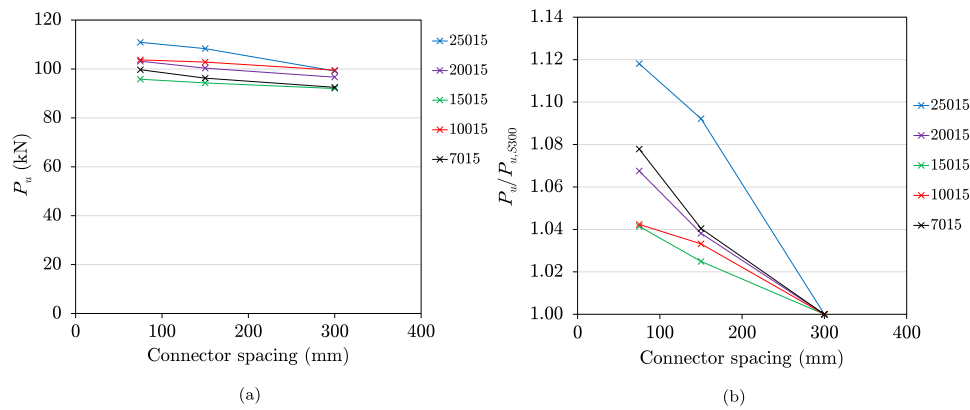


Fig. 26. Influence of connector spacing on ultimate compression capacity: (a) absolute values and (b) normalised by the compression capacity of the equivalent system with 300 mm connector spacing.

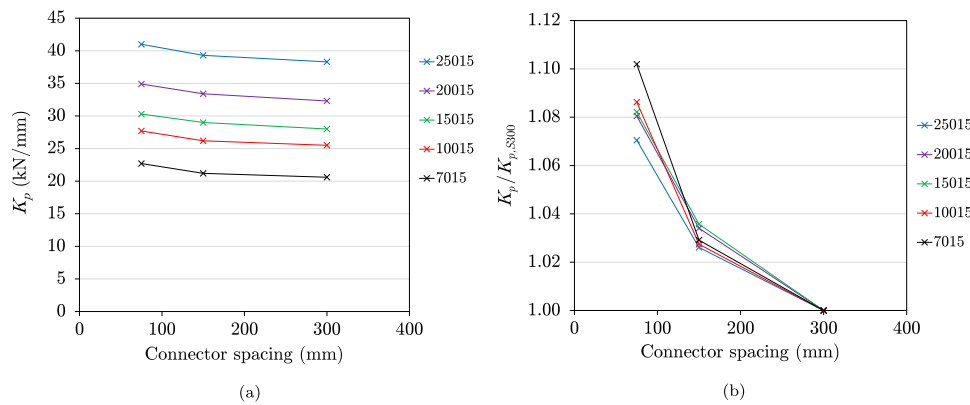


Fig. 27. Influence of connector spacing on measured initial axial stiffness: (a) absolute values and (b) normalised by the stiffness of the equivalent system with 300 mm connector spacing.

where the ultimate capacity P_u and initial stiffness K_p of each system is presented both in absolute values and normalised by the capacity and stiffness of the equivalent system with the widest (i.e. 300 mm) spacing of connectors ($P_{u,S300}$ and $K_{p,S300}$ respectively). Up to 12% increases in strength and 10% increases in stiffness were achieved for the systems employing the closest connector spacing (i.e. 75 mm) — see Figs. 26 and 27 respectively. As shown in Figs. 25 and 26, the ultimate capacity P_u was not significantly affected by changes in section depth as local buckling limits the capacity of the specimens with the more slender cross-sections [47].

4.2.2. Bending results

The horizontal load–displacement curves of all specimens under bending alone are presented in Fig. 28. As expected, the bending stiffness and ultimate bending capacity (indicated in terms of the ultimate horizontal load H_u) were found to increase with increasing section depth, with up to four times higher strength and 13 times higher stiffness achieved when increasing the section depth from 68 mm to 252 mm. The maximum horizontal load H_u and initial flexural stiffness K_p attained by each specimen are presented in Figs. 29 and 30 respectively, both in absolute values and normalised by the maximum

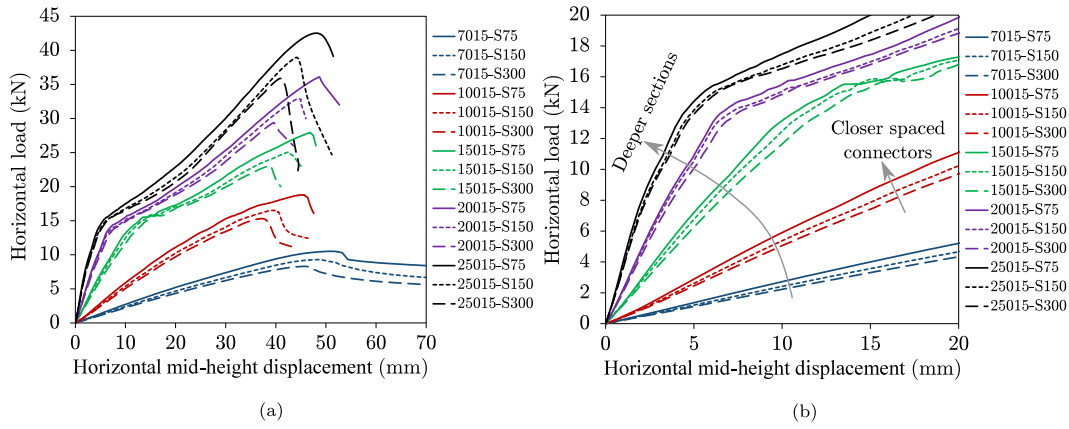


Fig. 28. FE parametric results of horizontal load vs mid-height deflections: (a) full spectrum and (b) initial detail.

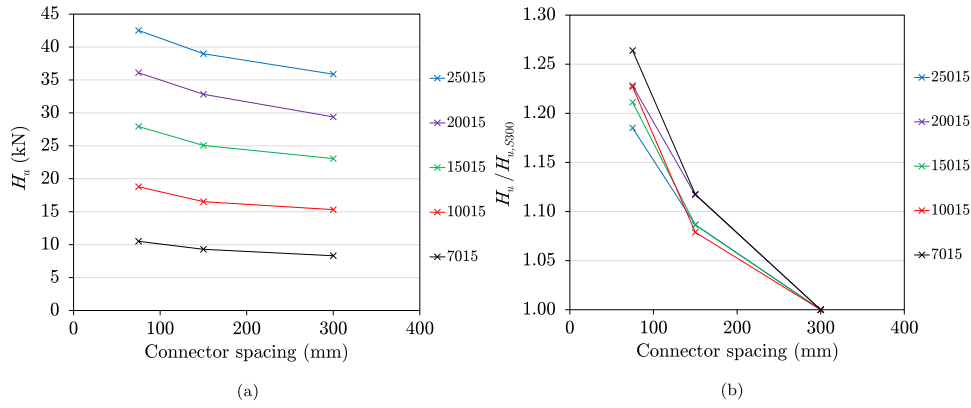


Fig. 29. Influence of connector spacing on ultimate bending capacity in terms of horizontal loads H_u : (a) absolute values and (b) normalised by the ultimate loads of the equivalent system with 300 mm connector spacing.

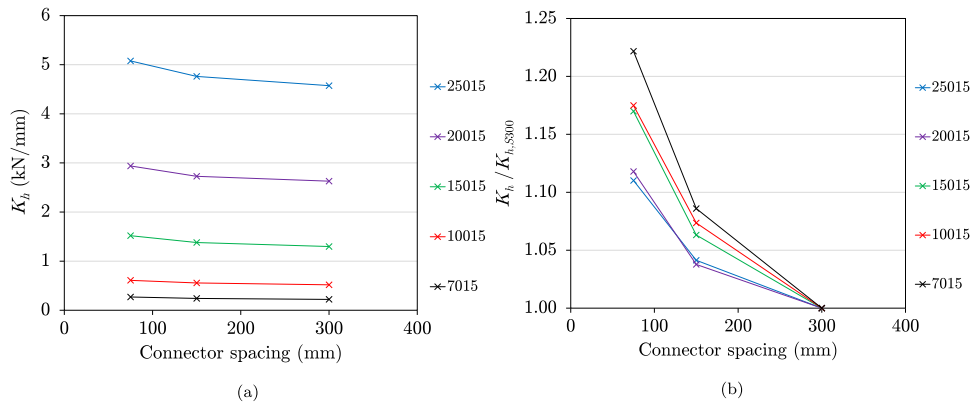


Fig. 30. Influence of connector spacing on flexural stiffness for the examined systems under bending: (a) absolute values and (b) normalised by the stiffness of the equivalent system with 300 mm connector spacing.

horizontal load and stiffness of the equivalent specimen with the widest (i.e. 300 mm) screw spacing ($H_{u,S300}$ and $K_{b,S300}$ respectively). Up to 26% increases in horizontal capacity H_u and 22% increases in bending stiffness K_b were achieved by decreasing the connector spacing from 300 mm to 75 mm, largely due to the effects of composite action – see Figs. 29 and 30 respectively.

A pronounced change in gradient can be observed in Fig. 28 for the specimens with a depth equal to or deeper than 150 mm at a load level of a 15 kN; this was caused by localised material yielding and buckling at the stud ends, as verified in Fig. 31. The effect of the end track on the behaviour of sheathed cold-formed steel members is discussed further in Section 4.3.

4.2.3. Combined loading results

The FE results of the specimens subjected to combined loading (i.e. axially loaded up to a percentage of the compressive capacity of the stud and then laterally loaded until failure) are reported in terms of axial load P_u and ultimate horizontal load H_u in Table 9. It is apparent that the $P_u - H_u$ relationship is not linear, since the specimens initially loaded up to 25%, 50% and 75% of P_u failed at about 90%, 70% and 40% respectively of the ultimate horizontal load H_u attained when under bending alone. The capacities of the specimens under combined loading were found to increase with decreasing connector spacing and increasing section depth, while the influence of the section

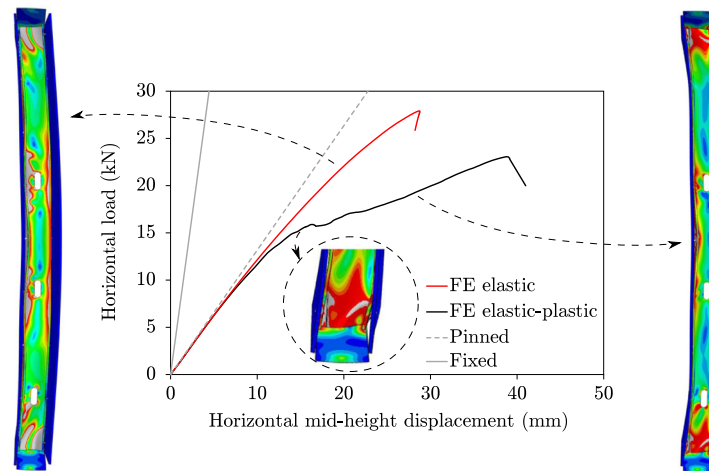


Fig. 31. Comparison of specimen 15015-S300 under bending modelled with (i) elastic and (ii) elastic-plastic material behaviour.

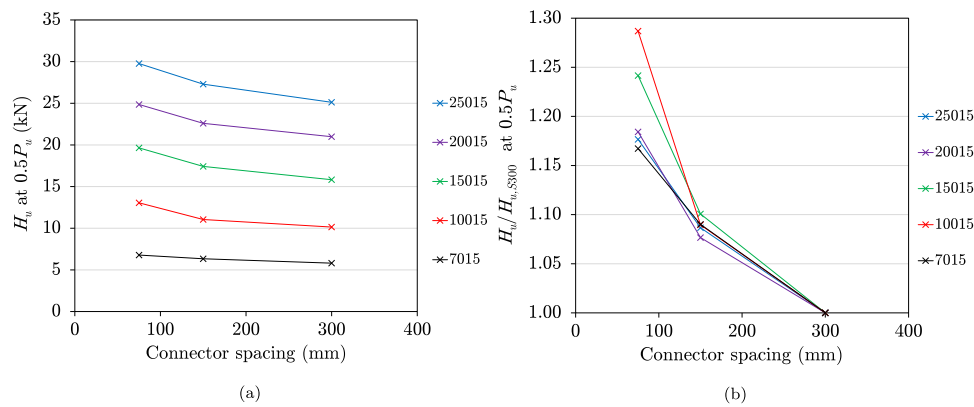


Fig. 32. Influence of connector spacing on bending capacity for specimens initially compressed to 50% of their compression capacity, in terms of horizontal loads H_u : (a) absolute values and (b) normalised by the loads of equivalent systems with a 300 mm connector spacing.

depth was found to be higher for lower levels of initial compression. A typical example of the influence of the connector spacing on the ultimate horizontal capacity H_u is provided in Fig. 32, where capacity improvements of up to 29% were achieved when shifting to closer spaced connectors (from 300 mm to 75 mm) for the specimens initially compressed to 50% of P_u .

The ultimate interaction curves for all of the examined specimens under combined loading are presented in Fig. 33, where the ultimate compressive load P_u is plotted against the ultimate horizontal load H_u , in terms of absolute values.

In order to examine more clearly the influence of the connector spacing on the response of specimens of different section depths, the ultimate interaction curves for each cross-section are plotted separately and presented in a normalised format in Fig. 34, using Eqs. (6) and (7), where $N_{c,Rk}$ is the axial cross-section resistance in compression, A_{eff} is the effective area in compression and f_y is the yield strength. In Eq. (7), $H_{c,y,Rk}$ is the horizontal load resistance corresponding to pinned boundary conditions, $M_{c,y,Rk}$ is the moment resistance about the major axis and $W_{eff,y}$ is the elastic section modulus of the effective cross-section about the major axis. Note that the effective section properties were calculated using the effective width method, in accordance with the provisions in Eurocode 3-1-3 [47].

$$N_{c,Rk} = A_{eff} f_y \tag{6}$$

$$H_{c,y,Rk} = M_{c,y,Rk} \times 8/L = W_{eff,y} f_y \times 8/L \tag{7}$$

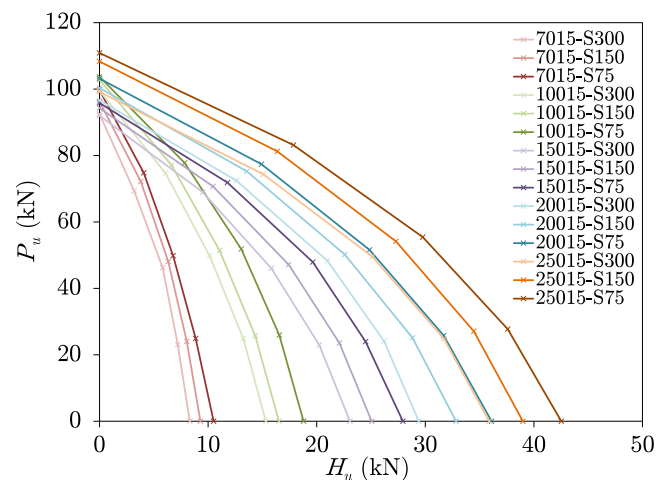


Fig. 33. Ultimate interaction curves from FE parametric results, presented in terms of ultimate compressive capacity P_u vs ultimate horizontal load capacity H_u .

As illustrated in Fig. 34, all interaction curves are of a convex profile, with decreasing connector spacing resulting in increased capacities. This effect gets more pronounced as bending becomes the predominant loading action, with the $H_u/H_{c,y,Rk}$ values corresponding

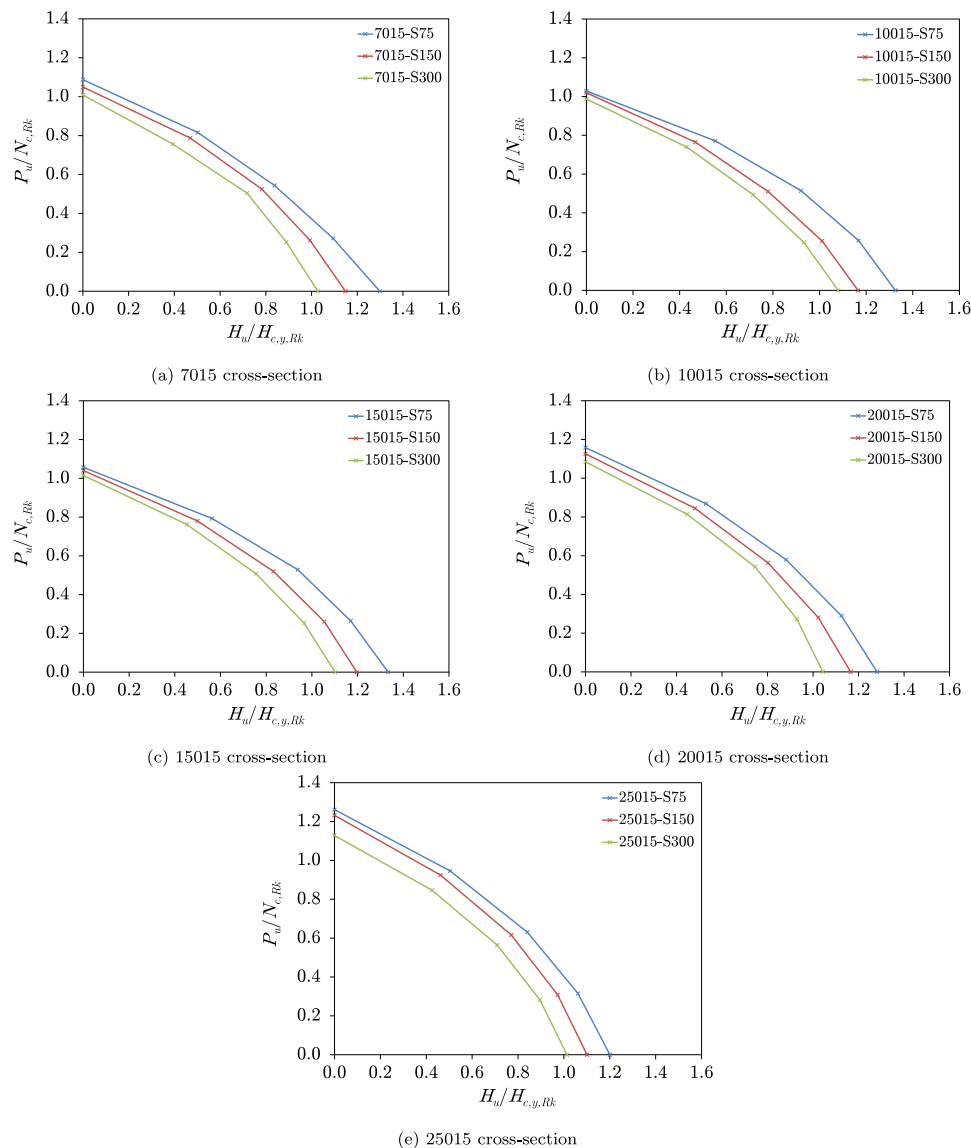


Fig. 34. Interaction curves from FE parametric results presented in terms of normalised capacities with effective cross-sectional properties determined using EN 1993-1-3 [47] plotted separately for each specimen with section depth: (a) 70 mm, (b) 100 mm, (c) 150 mm, (d) 200 mm and (e) 250 mm.

to bending alone shown to be greater than 1.0 for specimens connected at 300 mm intervals, then increasing to more than 1.1 for specimens with 150 mm connector spacings and, finally, for the specimens with 75 mm connector spacings, to values greater than 1.2. It should be noted that for section depths of more than 200 mm, the bending capacity starts to be limited by local buckling of the web.

4.3. Discussion on the effect of the track

Based on the parametric studies reported in Section 4.2, the tracks at the stud ends were found to affect the response of the sheathed stud wall specimens to different degrees depending on their geometric features as well as on the loading configuration. Under pure compression, the column-to-track boundaries behave almost like fully fixed connections, while when under bending alone, they behave like pinned connections — this has also been reported in experimental studies found in the literature [9,10,25]. When bending is predominant, the structural behaviour and failure mode of the examined systems are affected by the section depth, and, as a result, by the track depth. In Fig. 35, the failure modes of specimens of different section depths with 75 mm connector spacing under pure bending are presented. It can be

observed that for the two smaller sections, the main failure mode was local buckling at mid-height, while for the deeper specimens, localised buckling and yielding near the stud ends became dominant. For sections with a depth equal to or greater than 150 mm, the thickness of the track had to be increased to 2.5 mm in order to obtain a smooth load–displacement curve beyond the point at which the column ends started to fail. A stronger column-to-track connection was also required to not limit the system capacity. Therefore, the use of tracks of sufficient thickness in order to secure a smooth response not limited by the strength of the connection is recommended along with the use of a stronger connection between the column and the track, which can be achieved either with a larger diameter screw or by using more than one screw connector.

5. Conclusions

Finite element models simulating sheathed cold-formed steel studs set in tracks and subjected to various loading configurations (i.e. compression, bending and combinations of the two) were developed and validated against experimental data reported in the literature. The FE models included geometrical imperfections, while geometrical and

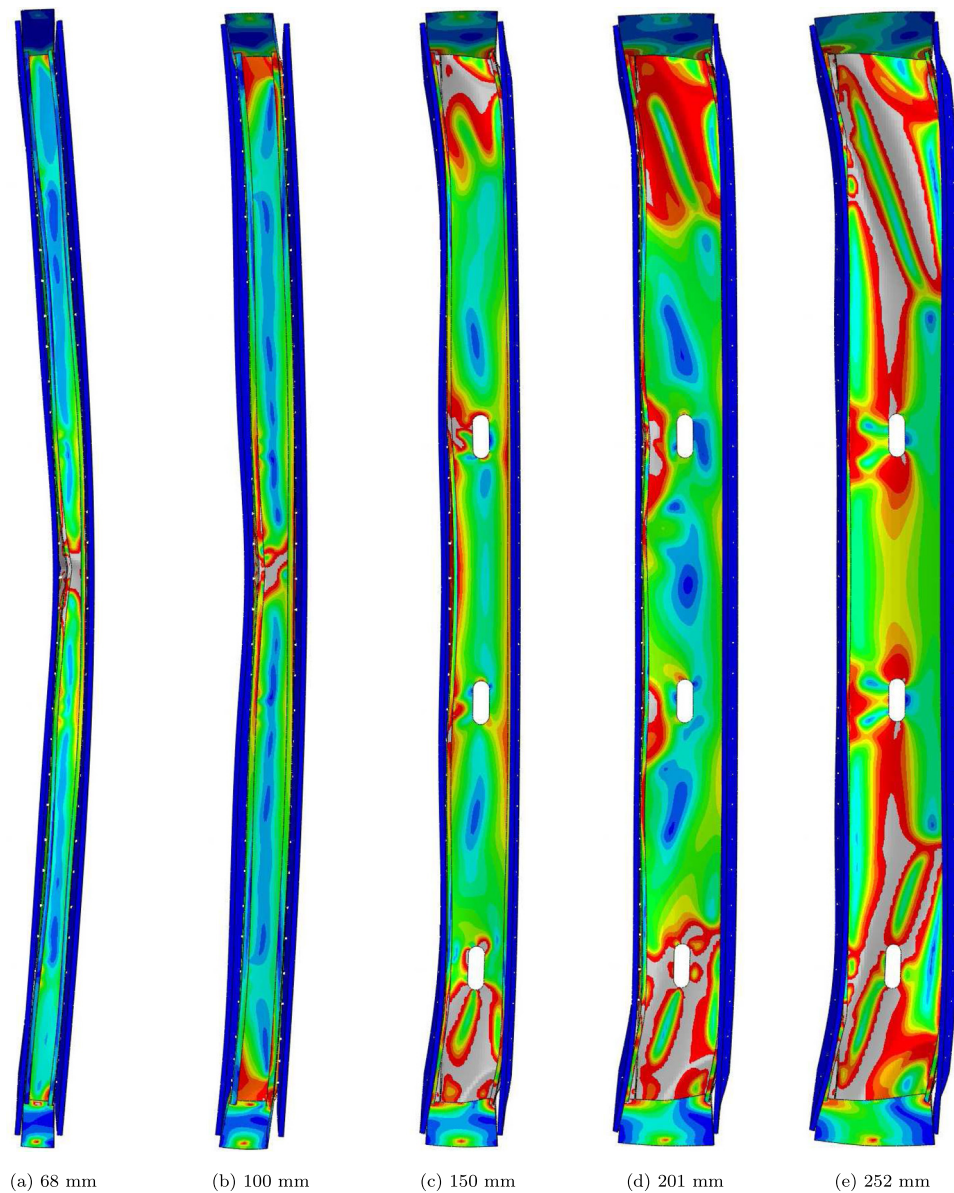


Fig. 35. Failure modes for specimens under bending alone with 75 mm screw spacing and a section depth of (a) 68 mm, (b) 100 mm, (c) 150 mm (d) 201 mm and (e) 252 mm.

material nonlinearities were also taken into account. The finite element simulations were found to be capable of realistically describing the column-to-track boundary conditions, while the contact interaction between the cold-formed steel columns and the boards, as well as the nonlinear behaviour of the employed connectors, were explicitly replicated.

Following successful validation, the FE models were employed to investigate the influence of the sheathing, section depth and fastener spacing on the load-bearing capacity of the columns under various loading scenarios. It was found that the addition of sheathing leads to significant increases in load-carrying capacities relative to bare steel columns; sheathing on both sides of the cold-formed steel studs with the more robust OSB panels led to about a 100% increase in capacity. The main reason for the gains in capacity is the restraint against the global buckling modes, while further increases due to closer connector spacing are attributed to a reduction of the wavelength of the distortional buckles and to the mobilisation of composite action between the boards and the column.

Decreasing the fastener spacing was found to lead to significant improvements in terms of ultimate capacity and stiffness under all

loading configurations, with up to 12% and 10% increases in capacity and stiffness respectively for specimens in pure compression, up to 26% and 22% increases in capacity and stiffness respectively for specimens in bending and up to a 29% increase in capacity for specimens under combined compression and bending when decreasing the connector spacing from 300 mm to 75 mm. Finally, the characteristics of the end tracks as well as the strength of the stud-to-track connections were found to have the potential to significantly affect the response of the examined systems, limiting their ultimate capacity. Recommendations on the choice of the end tracks and stud-to-track connection were therefore made to secure the efficient performance of sheathed cold-formed steel stud wall systems.

CRediT authorship contribution statement

Constantinos Kyprianou: Conceptualization, Methodology, Software, Validation, Formal analysis, Investigation, Data curation, Writing – original draft, Writing – review & editing, Visualization. **Pinelopi Kyvelou:** Writing – review & editing. **Leroy Gardner:** Conceptualization, Writing – review & editing, Supervision, Project administration. **David A. Nethercot:** Supervision.

Declaration of competing interest

The authors declare that they have no known competing financial interests or personal relationships that could have appeared to influence the work reported in this paper.

Data availability

Data will be made available on request.

Acknowledgements

Funding for this research was received from the EPSRC Centre for Doctoral Training in Sustainable Civil Engineering at Imperial College London (award reference: 1790029) and Ayrshire Metals.

References

- [1] R.M. Lawson, R.G. Ogden, 'Hybrid' light steel panel and modular systems, *Thin-Walled Struct.* 46 (7–9) (2008) 720–730.
- [2] G.G. Green, G. Winter, T.R. Cuykendall, *Light Gauge Steel Columns in Wall-Braced Panels*, (35 Part 2) Engineering Experiment Station, Cornell University, Ithaca, NY, USA, 1947.
- [3] A. Simaan, T. Peköz, Diaphragm braced members and design of wall studs, *J. Struct. Div. ASCE* 102 (1) (1976) 77–92.
- [4] T.H. Miller, T. Peköz, Behavior of gypsum-sheathed cold-formed steel wall studs, *J. Struct. Eng.* 120 (5) (1994) 1644–1650.
- [5] Y. Lee, T.H. Miller, Axial strength determination for gypsum-sheathed, cold-formed steel wall stud composite panels, *J. Struct. Eng.* 127 (6) (2001) 608–615.
- [6] Y. Telue, M. Mahendran, Behaviour and design of cold-formed steel wall frames lined with plasterboard on both sides, *Eng. Struct.* 26 (5) (2004) 567–579.
- [7] Y. Telue, M. Mahendran, Design of cold-formed steel wall frames lined with plasterboard on one side under axial compression, *Int. J. Steel Struct.* 6 (1) (2006) 1–12.
- [8] Y.S. Tian, J. Wang, T.J. Lu, Axial load capacity of cold-formed steel wall stud with sheathing, *Thin-Walled Struct.* 45 (5) (2007) 537–551.
- [9] L.C.M. Vieira Jr., B.W. Schafer, Behavior and design of sheathed cold-formed steel stud walls under compression, *J. Struct. Eng.* 139 (5) (2013) 772–786.
- [10] K.D. Peterman, B.W. Schafer, Sheathed cold-formed steel studs under axial and lateral load, *J. Struct. Eng.* 140 (10) (2014) 04014074.
- [11] D.C. Fratamico, B.W. Schafer, Numerical studies on the composite action and buckling behavior of built-up cold-formed steel columns, in: *22nd International Specialty Conference on Cold-Formed Steel Structures*, St. Louis, Missouri, USA, 2014, pp. 213–228.
- [12] S. Kechidi, D.C. Fratamico, B.W. Schafer, J.M. Castro, N. Bourahla, Simulation of screw connected built-up cold-formed steel back-to-back lipped channels under axial compression, *Eng. Struct.* 206 (2020) 110109.
- [13] R.M. Lawson, A.G. Way, M. Heywood, J.B.P. Lim, R. Johnston, K. Roy, Stability of light steel walls in compression with plasterboards on one or both sides, *Proc. Inst. Civ. Eng. Struct. Build.* (2019) 1–19.
- [14] P. Kyvelou, C. Kyprianou, L. Gardner, D.A. Nethercot, Challenges and solutions associated with the simulation and design of cold-formed steel structural systems, *Thin-Walled Struct.* 141 (2019) 526–539.
- [15] P. Kyvelou, D.A. Nethercot, N. Hadjipantelis, C. Kyprianou, L. Gardner, The evolving basis for the design of light gauge steel systems, *Int. J. Struct. Stab. Dyn.* 20 (13) (2020) 2041008.
- [16] M.-T. Chen, B. Young, A.D. Martins, D. Camotim, P.B. Dinis, Experimental investigation on cold-formed steel stiffened lipped channel columns undergoing local-distortional interaction, *Thin-Walled Struct.* 150 (2020) 106682.
- [17] M.-T. Chen, B. Young, A.D. Martins, D. Camotim, P.B. Dinis, Experimental investigation on cold-formed steel lipped channel beams affected by local-distortional interaction under non-uniform bending, *Thin-Walled Struct.* 161 (2021) 107494.
- [18] B. Young, *The Behaviour and Design of Cold-Formed Channel Columns* (Ph.D. thesis), University of Sydney, Sydney, Australia, 1997.
- [19] B. Young, K.J.R. Rasmussen, Design of lipped channel columns, *J. Struct. Eng.* 124 (2) (1998) 140–148.
- [20] B. Young, K.J.R. Rasmussen, Tests of cold-formed channel columns, in: *Fourteenth International Specialty Conference on Cold-Formed Steel Structures*, St. Louis, Missouri, USA, 1998.
- [21] S. Selvaraj, M. Madhavan, Bracing effect of sheathing in point-symmetric cold-formed steel flexural members, *J. Construct. Steel Res.* 157 (2019) 450–462.
- [22] L.C.M. Vieira Jr., B.W. Schafer, Fastener demands for sheathing-braced cold-formed steel stud gravity walls, *Lat. Am. J. Solids Struct.* 13 (6) (2016) 1167–1185.
- [23] C. Kyprianou, P. Kyvelou, L. Gardner, D.A. Nethercot, Characterisation of material and connection behaviour in sheathed cold-formed steel wall systems - Part 2: Analytical modelling, *Structures* 30 (2021) 1184–1199.
- [24] C. Kyprianou, P. Kyvelou, L. Gardner, D.A. Nethercot, Characterisation of material and connection behaviour in sheathed cold-formed steel wall systems - Part 1: Experimentation and data compilation, *Structures* 30 (2021) 1161–1183.
- [25] C. Kyprianou, P. Kyvelou, L. Gardner, D.A. Nethercot, Experimental study of sheathed cold-formed steel beam-columns, *Thin-Walled Struct.* 166 (2021) 108044.
- [26] C. Kyprianou, *Sheathed Cold-formed Steel Wall Systems* (Ph.D. thesis), Imperial College London, London, UK, 2021.
- [27] L.C.M. Vieira Jr., Y. Shifferaw, B.W. Schafer, Experiments on sheathed cold-formed steel studs in compression, *J. Construct. Steel Res.* 67 (10) (2011) 1554–1566.
- [28] L.C.M. Vieira Jr., *Behavior and Design of Sheathed Cold-Formed Steel Stud Walls Under Compression* (Ph.D. thesis), Johns Hopkins University, Baltimore, Maryland, USA, 2011.
- [29] K.D. Peterman, *Experiments on the Stability of Sheathed Cold-Formed Steel Stud Walls Under Axial Load and Bending* (Ph.D. thesis), Johns Hopkins University, Baltimore, Maryland, USA, 2012.
- [30] ABAQUS, Version 6.19, Dassault Systèmes Simulia Corp. Johnston, RI, USA, 2016.
- [31] B. Young, J. Yan, Finite element analysis of cold-formed channel columns, in: *Fifteenth International Specialty Conference on Cold-Formed Steel Structures*, St. Louis, Missouri, USA, 2000.
- [32] P.B. Dinis, D. Camotim, N. Silvestre, FEM-based analysis of the local-plate/distortional mode interaction in cold-formed steel lipped channel columns, *Comput. Struct.* 85 (19–20) (2007) 1461–1474.
- [33] C. Yu, B.W. Schafer, Simulation of cold-formed steel beams in local and distortional buckling with applications to the direct strength method, *J. Construct. Steel Res.* 63 (5) (2007) 581–590.
- [34] N. Hadjipantelis, L. Gardner, M.A. Wadee, Finite-element modeling of prestressed cold-formed steel beams, *J. Struct. Eng.* 145 (10) (2019) 04019100.
- [35] P. Kyvelou, L. Gardner, D.A. Nethercot, Finite element modelling of composite cold-formed steel flooring systems, *Eng. Struct.* 158 (2018) 28–42.
- [36] X. Yun, L. Gardner, Stress-strain curves for hot-rolled steels, *J. Construct. Steel Res.* 133 (2017) 36–46.
- [37] W. Ramberg, W.R. Osgood, Description of stress-strain curves by three parameters, *Technical Notes*, (902) National Advisory Committee for Aeronautics, Washington, 1943.
- [38] X. Yun, L. Gardner, The continuous strength method for the design of cold-formed steel non-slender tubular cross-sections, *Eng. Struct.* 175 (2018) 549–564.
- [39] C. Petrone, G. Magliulo, G. Manfredi, Mechanical properties of plasterboards: experimental tests and statistical analysis, *J. Mater. Civ. Eng.* 28 (11) (2016) 04016129.
- [40] J.B. Mander, M.J.N. Priestley, R. Park, Theoretical stress-strain model for confined concrete, *J. Struct. Eng.* 114 (8) (1988) 1804–1826.
- [41] C. Kyprianou, P. Kyvelou, L. Gardner, D.A. Nethercot, Numerical study of sheathed cold-formed steel columns, in: *Proceedings of the Ninth International Conference on Advances in Steel Structures*, Hong Kong, China, 2018.
- [42] H.C. Ho, K.F. Chung, Analytical prediction on deformation characteristics of lapped connections between cold-formed steel Z sections, *Thin-Walled Struct.* 44 (1) (2006) 115–130.
- [43] Z. Li, B.W. Schafer, Buckling analysis of cold-formed steel members with general boundary conditions using CUFISM: conventional and constrained finite strip methods, in: *Twentieth International Specialty Conference on Cold-Formed Steel Structures*, St. Louis, Missouri, 2010.
- [44] X. Zhao, *Measurement and Application of Geometric Imperfections in Cold-Formed Steel Members* (Ph.D. thesis), Johns Hopkins University, Baltimore, Maryland, USA, 2016.
- [45] N.J.S. Gorst, S.J. Williamson, P.F. Pallett, L.A. Clark, *Friction in Temporary Works*, Research Report, (71) University of Birmingham, Birmingham, U.K, 2003.
- [46] V.M. Zeinoddini, B.W. Schafer, Simulation of geometric imperfections in cold-formed steel members using spectral representation approach, *Thin-Walled Struct.* 60 (2012) 105–117.
- [47] EN 1993-1-3, *Eurocode 3: Design of Steel Structures — Part 1-3: General Rules — Supplementary Rules for Cold-Formed Members and Sheeting*, European Committee for Standardization, Brussels, Belgium, 2006.